Title

Prion-protein induced toxic signaling in the brain of a novel knock-in mouse model: A histopathological analysis

Author

Chen, Joy

Publication Date

2021

Peer reviewed|Thesis/dissertation

UNIVERSITY OF CALIFORNIA SAN DIEGO

Prion-protein induced toxic signaling in the brain of a novel knock-in mouse model: A histopathological analysis

A Thesis submitted in partial satisfaction of the requirements for the degree

Master of Science

in

Biology

by

Joy Chen

Committee in charge:

Professor Christina Sigurdson, Chair
Professor Gulcin Pekkurnaz, Co-Chair
Professor Cory Root

2021

The Thesis of Joy Chen is approved, and it is acceptable in quality and form for publication on microfilm and electronically.

University of California San Diego

2021

TABLE OF CONTENTS

LIST OF FIGURES

ACKNOWLEDGEMENTS

I would like to give my deepest appreciation to my committee chair, Dr. Christina Sigurdson, who has continually encouraged and guided me throughout this past year. I would also like to thank Dr. Don Pizzo, for performing the beautiful stains for me to quantify and providing me all the knowledge I have in histology. Thank you for all your patience and support as this would not have been possible without you two.

ABSTRACT OF THE THESIS

Prion-protein induced toxic signaling in the brain of a novel knock-in mouse model: A histopathological analysis

by

Joy Chen

Master of Science in Biology

University of California San Diego, 2021

Professor Christina Sigurdson, Chair
Professor Gulcin Pekkurnaz, Co-Chair

PrP^C reportedly binds toxic oligomers and transduces toxic signals to advance neurodegeneration. However, the neurotoxic mechanism of PrP^C signaling remains poorly understood. A new *Prnp* knock-in mouse model with a G93N substitution results in mice exhibiting severe kyphosis, ataxia, and seizures, with terminal disease observed as soon as postnatal day 25 (p25). Histologically, terminal brains display neurodegeneration and striking spongiform encephalopathy in the absence of aggregates. In this study, we assess how the addition of an N-terminal glycan to PrP^C causes pathology in $Prnp^{93N}$ mice brains over time. $Prnp^{93N}$ brains were studied using immunohistochemistry (IHC) to label astrocytes, microglia, oligodendrocytes, oligodendrocyte precursors (OPCs), and neurons. Hematoxylin and eosin (HE) stains were used for scoring brain lesions to determine whether the $Prnp^{93N}$ mouse model develops spongiform encephalopathy (SE) consistent with bonefide prion disease. Starting at p15, the $Prnp^{93N}$ hippocampus and thalamus had a greater SE score compared to WT, and the SE scores increased gradually as the disease progressed. There were also prominent endothelial cells and neutrophils packed in the blood vessels of the $Prnp^{93N}$ hippocampi from p20-p25. IHC stains of $Prnp^{93N}$ hippocampi revealed a striking loss of CA1 pyramidal neurons as early as p20, and progressively worsening microgliosis and astrogliosis starting at p10. This

thesis provides an in depth characterization of histopathology of the novel *Prnp*^{93N} mouse model where G93N substitution in PrP^{C} results in N-terminal-mediated toxic signaling that gives rise to the rapid onset of a developmental and spontaneous neurodegenerative disease in mice.

INTRODUCTION

I. Cellular Prion Protein

a. PrP^C Structure

The cellular prion protein (PrP^C) consists of 253 amino acids and is encoded by 16 kb on chromosome 20 in humans. The gene is referred to as *PRNP* (Imran et al., 2011). PrP^C contains an unstructured N-terminal domain consisting of residues 90-127 and a folded, globular C-terminal domain consisting of residues 128-228. The C-terminal globular domain contains a hydrophobic core, three alpha helices, and one short beta sheet with two antiparallel strands (Chen et al., 2014). Post-translational modification include the glycosylphosphatidylinositol (GPI) anchor at serine 231 in the C-terminal domain, attaching PrP^C to the outer surface of cell membranes (Stahl, 1993). The N-terminal domain contains the octapeptide repeats, a sequence of eight positively charged peptide repeats, known to bind copper(II) (Chen et al, 2014) (Lehmann et al., 2002) (Millhauser et al., 2007). A disulfide bond connects the two cysteine residues at position 179 and 214 in the C-terminal domain. Furthermore, up to two glycans can be added to asparagine at positions 181 and 197 in the N-terminus, with each glycan carrying up to five molecules of sialic acid (Stahl et al., 1993)(Rudd et al., 1999) (Katorcha et al., 2015).

b. PrP^C Function

PrP^C is expressed in neurons and glial cells in the CNS as well as in other cells in the peripheral organs including lymph nodes, heart, liver, and lungs (Zhang et al., 2020) (Ning et al., 2005). Although the exact function of PrP^C remains unclear, studies have reported that PrP^C is involved in important cellular developmental processes, including myelination and neuronal differentiation (Steele et al., 2006) (Nishida et al., 1999). PrP^C has also been shown to play neuroprotective roles as PrP^C deletion in mice results in neuronal damage [see Baumann and Aguzzi] (Onodera et al., 2014). PrP^C has also been proposed to bind copper (II) to reduce its deleterious redox abilities and decrease doppel-mediated apoptosis (Millhauser et al., 2007) (Walter et al., 2006) (Drisaldi et al., 2004). Furthermore, PrP^C is also thought to regulate intracellular calcium levels by interacting with ionotropic glutamate receptors such as N-methyl-D-aspartate receptor (NMDAR). Mice with less PrP^C have an increased expression of a NMDAR subunit associated with excitotoxicity (Pham et al., 2014).

Aside from developmental and neuroprotective properties, PrP^C is also thought to play a role in neurotoxic processes by binding to extracellular ligands to transduce intracellular signaling. In prion disease, PrP^C is necessary

for mediating toxic effects of prion aggregates (PrP^{Sc}) as transgenic PrP^{C} knockout animals have an absence of PrP^{Sc} neurotoxicity (Salvesen et al., 2020) (Weissmann et al., 1993) (Brandner et al., 1996) (Mallucci et al., 2003). Other studies have also shown that PrP^{C} binds to other toxic aggregates such as alpha synuclein, amyloid beta (Aß), and tau oligomers (Watts et al., 2017). Interestingly, different intracellular cascades are triggered by different oligomers (Le et al., 2019). Thus, PrP^{C} may act as a common receptor for different oligomers, transducing different intracellular signals in prion and other neurodegenerative diseases.

c. N-Terminus Toxicity

Since PrP^{C} is thought to be involved in toxic signaling, specific regions have been identified as necessary for toxic signaling. One study showed that treatment with N-terminal-specific ligands, including antibodies, sulfated glycosaminoglycans, and copper (II), resulted in inhibition of the spontaneous excitotoxic currents (Wu. Et al, 2017). Specifically, the octapeptide repeat domain was shown to be necessary for ion channel activity, as its deletion abolished neurotoxicity (Solomon et al., 2011) (Wu et al., 2017). To determine N-terminal regulation, treatment with C-terminal-specific antibodies were found to lead to excitotoxic current in cells with WT PrP^{C} (Wu et al., 2017). It was proposed that the N-terminal domain is regulated by C-terminal domain through usage of copper (II) which has a high affinity to the octapeptide repeat domain in the N-terminus. A study has shown that the C-terminal domain actually carries a pocket of negative charge that is thought to bind to copper(II) on the N-terminal domain, inhibiting the toxic effects (Evans et al., 2016). In summary, these studies have shown that the N-terminal domain is the autonomous toxic effector responsible for the neurotoxicity, which may contribute to neuronal loss in prion and other neurodegenerative diseases.

d. Mechanism of Toxic Signal Transduction

After the binding of a toxic aggregate, there is activation of the N-terminal domain of PrP^{C} and intracellular toxic signaling is initiated (Le et al., 2019). Exactly how this toxic signaling occurs has yet to be resolved. One hypothesis is that toxicity involves altering glutamate receptors, such as NMDA and AMPA, and the notion of glutamate-mediated excitotoxicity has been supported by studies showing PrP^{Sc}-mediated intracellular calcium influx in neurons (REF). By treating the neurons with NMDA and AMPA receptor blockers, neurons are protected from excitotoxic insult and excitotoxic phenotypes are reversed (Fang et al., 2018). Studies have also shown that

PrP^{Sc} interacts, modulates, and activates NMDA receptors and leads to significant calcium influx (Fang et al., 2018)(Black et al., 2014)(Khosravani et al., 2008) (Fischer et al., 2000).

II. Astrocytes in Health & Disease

Astrocytes are the most abundant glial cell in the brain, comprising approximately 25% of brain volume (Tower et al., 1973). Astrocytes are involved in regulating glutamate homeostasis, buffering ions, communicating with other glial cells and neurons, and maintaining blood brain barrier (BBB) integrity (Yang et al., 2013). Astrocytes are generated from neuronal stem cells and peak astrogenesis ranges from embryonic day 18 (E18) to P7 in rodents (Tien et al., 2012) (Sauvageot et al., 2002). Mature astrocytes develop abundant peripheral astrocyte processes (PAPs) around P14-P26. PAPs function by increasing surface area for important membrane proteins including ion channels, transporters, and receptors that allow for optimal astrocyte function (Yang et al., 2013). One important membrane protein is the glutamate transporter (GLT1/GLAST) responsible for clearing extracellular glutamate (Yang et al., 2013). Ultimately, the loss of PAPs containing essential membrane proteins may result in astrocyte dysfunction and contribute to developmental and neurodegenerative diseases.

Astrocytes have been hypothesized to develop either neurotoxic or neuroprotective activation states depending on environmental stimuli (Liddelow et al, 2017). Neuroprotective roles of activated astrocytes include recognizing and phagocytosing aggregates, such as PrP^{Sc}, and increasing cytokine expression to attract microglia to an area of insult (Marella et al., 2004). However, if astrocytes are activated by microglial inflammatory cytokines, they will develop a neurotoxic phenotype, in which homeostatic functions are lost and death of oligodendrocytes and neurons is induced (Liddelow et al., 2017).

Reactive astrocyte morphologies consist of a reactive phenotype and astrodegenerative phenotype (Verkhratsky et al., 2020). The reactive astrocyte phenotype exhibits increased GFAP (glial fibrillary acidic protein) expression and a hypertrophied cell body (Verkhratsky et al., 2020). The astrodegenerative phenotype is characterized by decreased astrocyte density due to increased astrocyte death and extreme swelling of the cell body accompanied loss of PAPs (Escartin et al., 2021) (Verkhratsky et al., 2020). Due to the loss of PAPs and decrease in astrocyte number, astrodegenerative phenotypes are also accompanied by impaired astrocytic homeostatic functions. The astrodegenerative phenotype has been observed in trauma-induced, ischemic, aged, and psychiatric diseased brains (Tachibana et al., 2019).

III. Microglia Biology in Health & Disease

Microglia are resident macrophages in the brain that make up from 5 to 15% of adult brain cells (Thion et al., 2018). Microglia are important for normal brain development as they are responsible for phagocytosing synapses, axons, and apoptotic cells. They are also involved in neurogenesis, axon targeting, synapse formation, and other important cellular processes through secretion of diffusible factors (Thion et al., 2018). Microglia originate from the yolk sac and colonize the brain from E9 to P7 in rodents (Li et al., 2019) (Salter et al., 2017). Microglia numbers peak at P14 and then decrease as adult microglia numbers are set around P28 (Lenz et al., 2018) (Kim et al., 2015) (Nikodemova et al., 2014). Mature microglia are long-lived and self-renew under normal homeostatic conditions (Thion et al., 2018). However, microglial longevity increases vulnerability to early inflammation events that can lead to long-term microglial dysfunction (Datta et al., 2018).

Activated microglia can be categorized into subtypes: M1 pro-inflammatory or M2 anti-inflammatory. They can also adopt different morphologies depending on environmental stimuli. M2 anti-inflammatory microglia promote tissue healing through secretion of molecules such as insulin-like growth factor 1 (IGF1), while M1 pro-inflammatory subtype promote neuroinflammation through secretion of pro-inflammatory cytokines including tumor necrosis factor-alpha (TNF-alpha) and interleukin 1ß (IL-1ß) (Tang et al., 2016). The “resting” microglial morphology is characterized by a small soma and long, thin processes (Colonna et al., 2017). The intermediate state of activated microglia is characterized by slightly enlarged soma and short processes. The amoeboid microglia have very short or nonexistent processes and is in an amoeboid shape to optimally mobilize to sight of infection and phagocytose foreign pathogens (Schwarz et al., 2012). The round microglia are the most activated state of microglia and exhibit a round morphology with no processes (Lehrmann et al., 1997).

IV. Oligodendrocyte Biology in Health & Disease

Oligodendrocytes are the myelinating cells in the CNS that make up about 5-10% of the total glial population (Barateiro et al., 2016). The main function of oligodendrocytes is to generate myelin, a lipid membrane that wraps around axons for efficient conductance of action potentials. Myelin is necessary for neuronal health, as mice deficient in mature myelin show spontaneous neurodegeneration (Uschkureit et al., 2000). Oligodendrocytes have a high vulnerability to insults due to their expression of NMDA, AMPA (alpha-amino-3 hydroxy-5-methyl-4-isoxazolepropionic acid), kainate, and ATP receptors (P2X purinoreceptor-7) (McTigue et al., 2008) (Patel et al.,

2012) (Nutma et al., 2020). As a result, neuroinflammation involving activated astrocytes and microglia can lead to oligodendrocyte damage (Bezzi et al., 2001).

Though oligodendrocytes are extremely sensitive to insult, remyelination can occur to replace damaged oligodendrocytes. Remyelination is characterized by proliferation, migration, and differentiation of OPCs (Kipp et al., 2012). Though astrocytes can cause excitotoxic insult that damages oligodendrocytes, they can promote remyelination by secretion of chemokines :IL-1ß (interleukin 1 beta), CCL2 (C-C motif chemokine ligand 2), and FGF-2 (fibroblast growth factor 2) (van der Knaap et al., 2017) (Van Strien et al., 2011) (Franklin et al., 2017).

Knock-in Mice Expressing Prnp^{93N}

In the *Prnp*^{93N} knock-in mouse model, the amino acid glycine (G) was substituted for asparagine (N) in the 93 position of PrP^{C}, resulting in the addition of a third glycan in the disordered N-terminal domain close to the octapeptide repeat domain known to bind copper (II). These mice exhibit clinical signs of ataxia, hind leg clasp, kyphosis, tremors and histologically exhibit spongiform encephalopathy, gliosis, and spontaneous neurodegeneration in the absence of protein aggregates. The absence of protein aggregates was determined by RT-quick, histology, and biochemistry, by tracking PrP^{Sc}. *Prnp*^{93N} are also found to be non-infectious by inoculation *Prnp*^{93N} brain homogenates into mice.

Most studies suggest PrP^{C} mediated PrP^{Sc} toxicity is necessary for prion disease progression. However, *Prnp*^{93N} mice experience prion-like symptoms in the absence of infectious protein aggregates. This model uncouples spongiform encephalopathy from PrP^{Sc} and suggests a neurotoxic role of PrP^{C}.

Specific Aims

The question I am trying to address in this study is whether PrP^{C} toxic signaling can result in cellular dysfunction and neuronal death. Therefore I have characterized the normal development of astrocytes and microglia by studying WT (C57BL/6) mouse brains from p5 to p25. Next, I have extensively characterized the development in the *Prnp*^{93N} mouse brain by immunohistochemical labelling. To assess astrogliosis and microgliosis, I quantified GFAP and SOX9 (SRY-Box Transcription Factor 9) and Iba1 (ionized calcium binding adaptor molecule 1) immunolabelling, respectively, in *Prnp*^{93N} mice brains. To assess the pathology of oligodendrocytes and OPCs, I quantified Olig2 (Oligodendrocyte Transcription Factor 2) and NG2 (neural/glial antigen 2). To assess neuronal

loss, I quantified NeuN (neuronal nuclear protein) stains. To assess spongiform encephalopathy, HE (hematoxylin and eosin) stains were scored for spongiform changes from 0 to 3.

My key findings were that the *Prnp*^{93N} brain exhibits both a developmental and neurodegenerative disease phenotypes characterized by varying activation states of astrocytes and microglia as early as p10, spongiform changes as early as p15, increased oligodendrocyte and OPC numbers at p20, and massive neurodegeneration in the CA1 region of the hippocampus as early as p20.

METHODS

Animals

Prnp^{93N} mice were generated in the Sigurdson Laboratory. These *Prnp*^{93N} mice were backcrossed onto the C57/BL6 background. Mice were monitored daily to observe for clinical signs such as ataxia, hind leg clasp, kyphosis, and seizures.

Brain Preparation & IHC Staining

Brains were extracted and fixed in neutral buffered formalin. Tissue was processed into paraffin. Tissue sections were cut from blocks of formalin-fixed paraffin embedded brain tissue. Five-micron tissue sections were placed onto positively charged sialinized glass slides and stained with HE and the following IHC stains: GFAP and SOX9 for astrocytes (1:6000; DAKO) (1:3000; Abcam), Iba1 for microglia (1:3000; WAKO), Olig2 for oligodendrocytes (1:750; Abcam), NG2 for oligodendrocyte precursor cells (1:75; Abcam), NeuN for neurons (1:1500; Abcam), cleaved caspase-3 for apoptosis (1:900; Cell Signaling) Lamp1 for lysosomes (1:150; Developmental Studies Hybridoma Bank). All stains were performed on an automated tissue immunostainer (Ventana Discovery Ultra, Ventana Medical Systems, Inc). Most stains used heat-based antigen retrieval, performed using CC1 (Tris-EDTA based; pH 8.6) for 24-40 minutes at 95 ºC, except for GFAP, which used protease retrieval for 16 minutes. The primary antibodies were incubated on the sections for 32 minutes at 37 ºC. Primary antibodies were detected using the UltraMap or OmniMap systems (Ventana Medical system) depending upon the sensitivity needed, antibody was visualized using DAB as a chromagen followed by hematoxylin as a counterstain. Slides were rinsed, dehydrated through alcohol and xylene and coverslipped.

Scans

HE and all IHC stains were scanned on Zeiss AxioScan.Z1 (Carl Zeiss Microscopy LLC, White Plains, NY, USA) at 40x objective for maximal image resolution. AxioScan.Z1 uses the software Zen2 (Carl Zeiss Microscopy LLC, White Plains, NY, USA) for automatic thresholding and tissue detection. All brain sections on the slide were combined into a single image using the default stitching parameter.

Quantification of Stains

Scans containing ideal hippocampal cross-sections were hand selected and imported into Definiens Tissue Studio Software for quantification of each IHC stain (Definiens; Munich, Germany). Regions of interest (ROI) were manually drawn to analyze specific regions of the brain. ROIs studied in this project include hippocampus, cortex, and thalamus. Training subsets from ROIs were manually selected to test threshold values for DAB (3,3'-diaminobenzidine) and hematoxylin staining intensity. Once threshold values that optimally captured each IHC stain were decided, the software was used to analyze the stain in all ROIs and give a percent area and intensity reading for cytoplasmic stains or a positive nuclei count per area reading for nuclear stains. In addition to quantification readouts, image layouts for positive stains are also generated. For all stains, test runs were conducted to validate software quantification analysis. If the software did not accurately capture the stain, threshold values were changed and samples were run until validated.

SE Scoring

Preliminary study looking at HE of *Prnp*^{93N} terminal brain sections revealed striking SE. To localize the lesions and determine the timeline of lesion development, WT and *Prnp*^{93N} brains at timepoints p10 (WT n=3, *Prnp*^{93N} N=7), p15 (n=6, 4), p20 (n=3, 8), and p25 (n=3, 7) were collected, stained with HE, and scored for SE at 10x magnification. The following brain regions were analyzed in six regions including grey and white matter: the (1) cortex, (2) corpus callosum, (3) hippocampus, (4) thalamus, (5) hypothalamus, and (6) cerebral peduncle (Fig. 1A). SE was scored at 10X magnification according to size, multiplicity, and shape from 0-3 (0= less than 2 small vacuoles, 0.5=less than 10 scattered small vacuoles, 1=greater than 10 scattered small vacuoles, 1.5=greater than 10 small vacuoles and less than 5 scattered large vacuoles, 2=greater than 5 large vacuoles and 10 small vacuoles, 2.5=greater than 10 large vacuoles and 10 small vacuoles, 3=greater than 10 large vacuoles with some fusing

together and 10 small vacuoles). Examples of small, unfused vacuoles and large, fused vacuoles are given in Figure 1B. Brains were scored by Dr. Christina Sigurdson, DVM, PhD, of the Department of Pathology at UCSD School of Medicine and I, independently. Scorers were blinded to the genotypes of the mice and scoring results were consistent among evaluators. SE scores for each brain region of each individual animal were plotted on a scatter bar graph.

Western Blot

P20 cortex from six WT and six *Prnp*^{93N} mice were collected and homogenized for western blot analysis probing for GFAP. Homogenates were treated with complete lysis buffer containing 2% sarcosyl, phosphatase inhibitor PhosSTOP™ and protease inhibitor, and nucleic acid inhibitor Benzonase™, lysed on ice for 30 minutes. BCA was run to determine total protein in each sample. Samples were heat inactivated at 95C for 5 minutes. Samples were run through a NuPage Bis-Tris gel (Thermo Fisher Scientific) at 100V for 10 minutes and then 160V for 60-90 minutes. Samples were then transferred onto a nitrocellulose membrane by wet blotting for two hours and blocked in casein. Membranes were incubated in monoclonal antibody 1:2000 GFAP (DAKO z0334), then incubated in rabbit secondary antibody. 1:7000 GAPDH was used as a housekeeping gene (Novus Biologicals NB300-221SS). Blots were developed with a chemiluminescent substrate (Supersignal West Dura ECL, Thermo Fisher Scientific) and visualized on a Fuji LAS 400 imager. Multigauge V3 software (Fujifilm) was used to quantify GFAP.

Statistical Analysis

All data was analyzed using one-way ANOVA or two-way ANOVA with post-hoc Tukey test using GraphPad Prism v7 technology. Graphs were constructed with GraphPad Prism v7 technology.

RESULTS

Spongiform Encephalopathy (SE) in *Prnp*^{93N} Brains

Initial assessment of terminal *Prnp*^{93N} brains by HE, revealed striking SE and neurodegeneration. SE is a pathologic hallmark of prion disease, although it does not occur in all genetic forms of prion disease. To determine the extent and severity of SE in *Prnp*^{93N} terminal mice, we first scored the vacuoles in six brain regions: (1) cortex, (2) corpus callosum, (3) hippocampus, (4) thalamus, (5) hypothalamus, and (6) cerebral peduncle on a scale of 0-3 (3 being most severe). The highest scoring brain regions were the hippocampus and the thalamus.

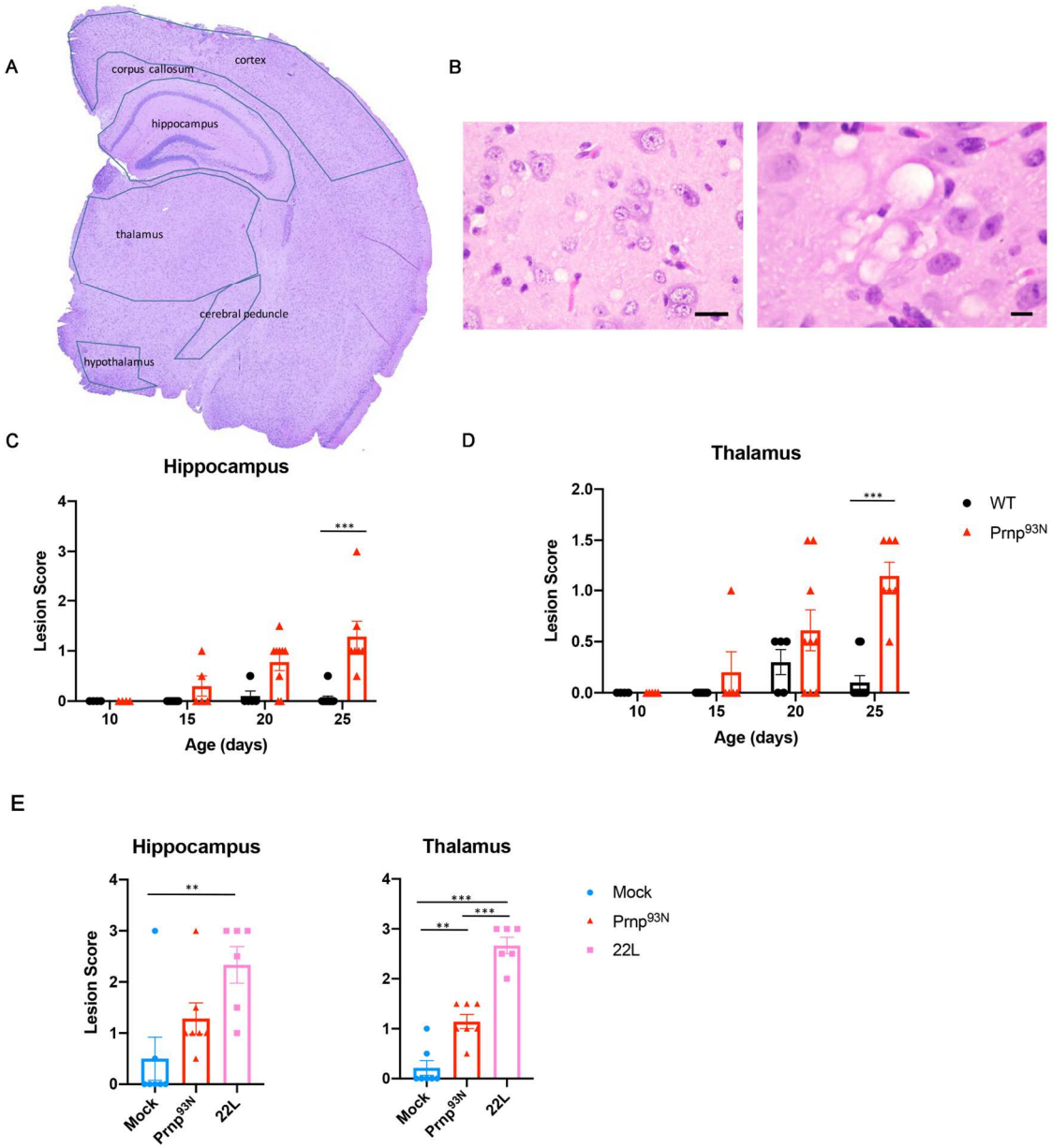

Figure 1. Spongiform encephalopathy in *Prnp*^{93N} brains. **(A)** HE of coronal brain section with regions of interests for lesion study mapped. **(B)** Examples of individual vacuoles on the left in 40x magnification with scale bar=50.0µm and fused vacuoles on the right in 60x magnification with scale bar=20.0µm. **(C)** Bar graph reveals WT and *Prnp*^{93N} hippocampal SE scores across timepoints p10 to p25. **(D)** Bar graph of WT and *Prnp*^{93N} thalamus SE scores from p10 to p25. Statistical comparisons of WT and *Prnp*^{93N} hippocampi and thalamus were performed by ordinary two-way ANOVA with post-hoc Tukey test (***=p<0.001). **(E)** Bar graph comparing SE scores of 22L inoculated, mock inoculated, and p25 *Prnp*^{93N} hippocampi and thalamus. Statistical comparisons of 22L, mock, and *Prnp*^{93N} hippocampi and thalamus were performed by ordinary one-way ANOVA with post-hoc Tukey test (**= p<0.002; ***=p<0.001).

Next, to determine timeline of SE development, *Prnp*^{93N} and wild type (WT) brains were taken at p10, p15, p20, and p25 and stained with HE. There was a significantly higher SE score in the *Prnp*^{93N} hippocampus and

thalamus compared to WT P25 (Fig. 1C, 1D). There is also a trend of increasing SE scores from p15 to p25 in *Prnp*^{93N} hippocampus and thalamus. No significant differences in SE scores were found in WT and *Prnp*^{93N} basal ganglia, cerebral cortex, hypothalamus, corpus callosum, brain stem, or cerebral peduncle. This data suggests that SE in the *Prnp*^{93N} hippocampus and thalamus occur as early as p15 and increase progressively as disease progresses. Furthermore, to compare the *Prnp*^{93N} mouse model with a bonefide prion disease, we compared SE scores from p25 *Prnp*^{93N} hippocampi to mock- and prion (22L)-inoculated. In the thalamus, *Prnp*^{93N} thalamus had an SE score significantly greater than that of mock, yet less than that of prion-inoculated brain. There was a higher SE score in prion (22L)-inoculated hippocampi when compared to mock (Fig. 1E). This data indicates that the *Prnp*^{93N} mice develops SE, although somewhat less than in a typical prion disease.

Neutrophils and Prominent Blood Vessels in *Prnp*^{93N} Brains

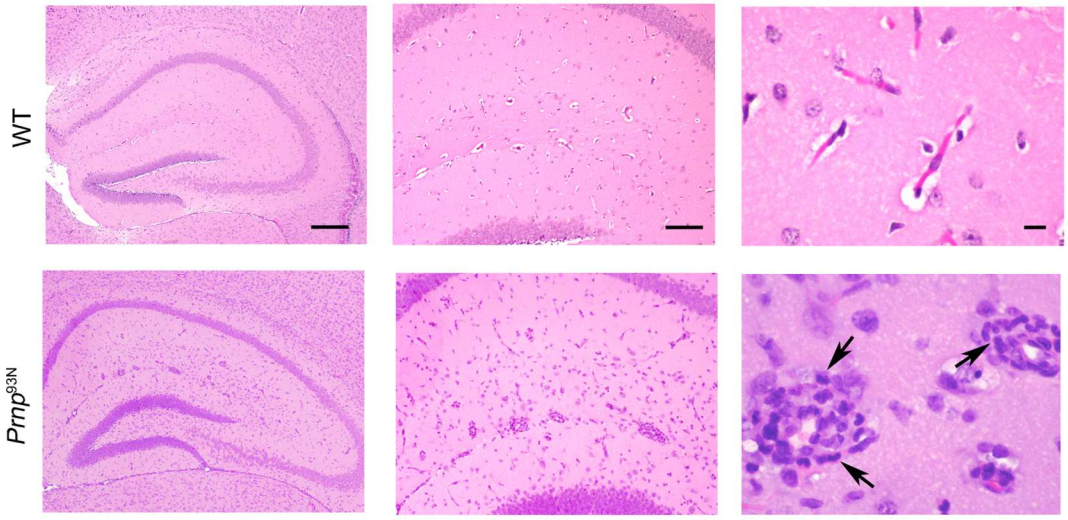

Figure 2. HE of p25 WT and *Prnp*^{93N} hippocampi reveals neutrophils and prominent blood vessels in the stratum radiatum, stratum laculosum moleculare, and molecular layer of dentate gyrus of the hippocampus. Scale bars = 500, 200, and 20.0µm from left to right.

HE stains of WT and *Prnp*^{93N} hippocampi reveal prominent endothelial cells in blood vessels in the stratum radiatum, stratum laculosum-moleculare, and the molecular layer of dentate gyrus as early as p15. We also observed the presence of neutrophils, which packed the blood vessel wall in the hippocampus and thalamus of approximately half of the *Prnp*^{93N} mice from ages p20 to p25. In contrast, the WT hippocampus was unremarkable with small blood vessels and an absence of neutrophils (Fig. 2).

Prnp^{93N} CA1 Neuronal Loss Starting at P20

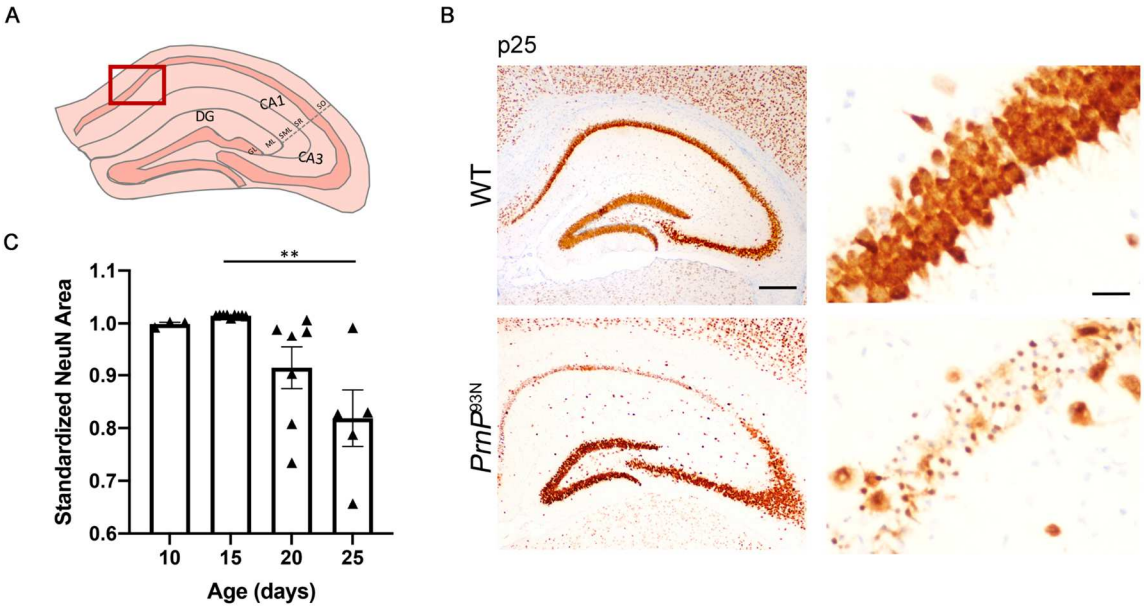

Figure 3. NeuN stain of *Prnp*^{93N} brains. **(A)** Hippocampal diagram of the exact region the following images were taken. **(B)** NeuN stain of p25 WT and *Prnp*^{93N} hippocampi reveal striking loss of neurons in CA1 region in *Prnp*^{93N} mice with scale bar = 500µm, 50.0µm from left to right. **(C)** Bar graph reveals *Prnp*^{93N} hippocampal NeuN data standardized by the average of WT NeuN data. WT NeuN data across all timepoints were insignificant. TissueStudio^{TM} quantification of NeuN reveals significant decrease in NeuN area from p15 to p25. Statistical comparisons of WT and *Prnp*^{93N} hippocampi were performed by ordinary one-way ANOVA with post-hoc Tukey test (**= $p<0.002$).

To assess neuronal loss in the brain, NeuN stain was performed and evaluated in the CA1 region of the hippocampus, cerebral cortex, and thalamus. No significant differences in WT hippocampal NeuN were found across timepoints. *Prnp*^{93N} NeuN revealed no neuronal loss in CA1 region of *Prnp*^{93N} hippocampi at p10 and p15 (Fig. 3C). Starting at P20, there is a trend of decreasing NeuN area in CA1 soma of *Prnp*^{93N} hippocampi and a significant decrease of NeuN area in CA1 soma at p25. No significant differences in NeuN were found in cerebral cortex or thalamus comparing WT and *Prnp*^{93N} brains across all timepoints. Thus, *Prnp*^{93N} mice show around 25% neuronal loss in the CA1 region of hippocampus starting at P20 and 50% neuronal loss by P25.

Apoptosis, Not the Mechanism of *Prnp*^{93N} Cell Death

Cleaved Caspase-3 Staining at p25

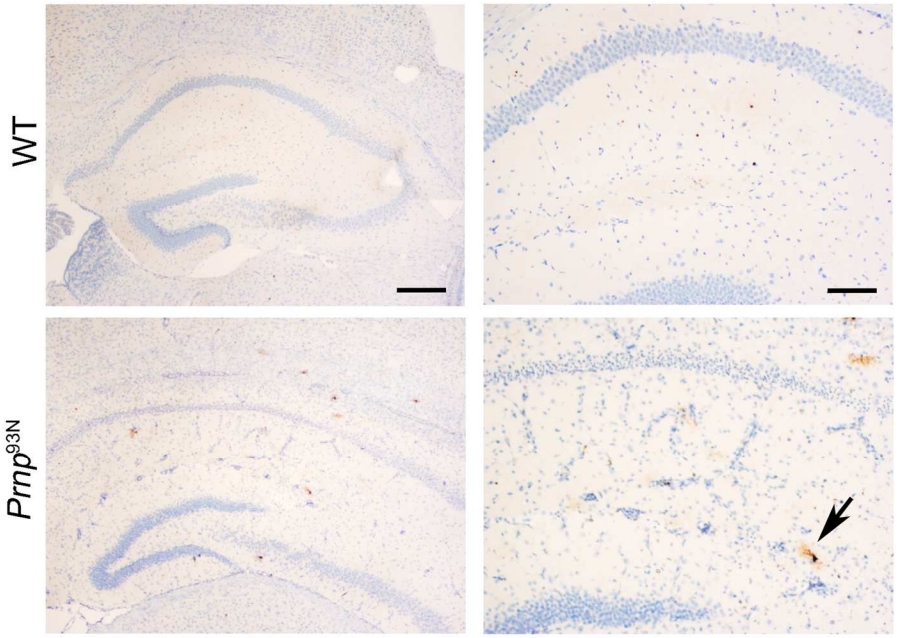

Figure 4. Cleaved caspase-3 stain of p25 *Prnp*^{93N} and WT hippocampi were stained with cleaved caspase-3. There was minimal staining of both WT and *Prnp*^{93N} hippocampi. Arrow points to possible positive cleaved caspase-3-stained cell. Scale bar=500, 200µm from left to right.

To determine the mechanism of neuronal death, *Prnp*^{93N} and WT brains were immunolabeled for cleaved caspase-3, an apoptotic cell marker (Fig. 4). Minimal positive stain for cleaved caspase-3 suggested apoptosis may not be the main mechanism of neuronal death in *Prnp*^{93N} hippocampi and further ultrastructural studies performed in the laboratory revealed a necrosis phenotype (Unpublished data, 2021).

Olig2 Timecourse: Oligodendrocytes in the Hippocampus

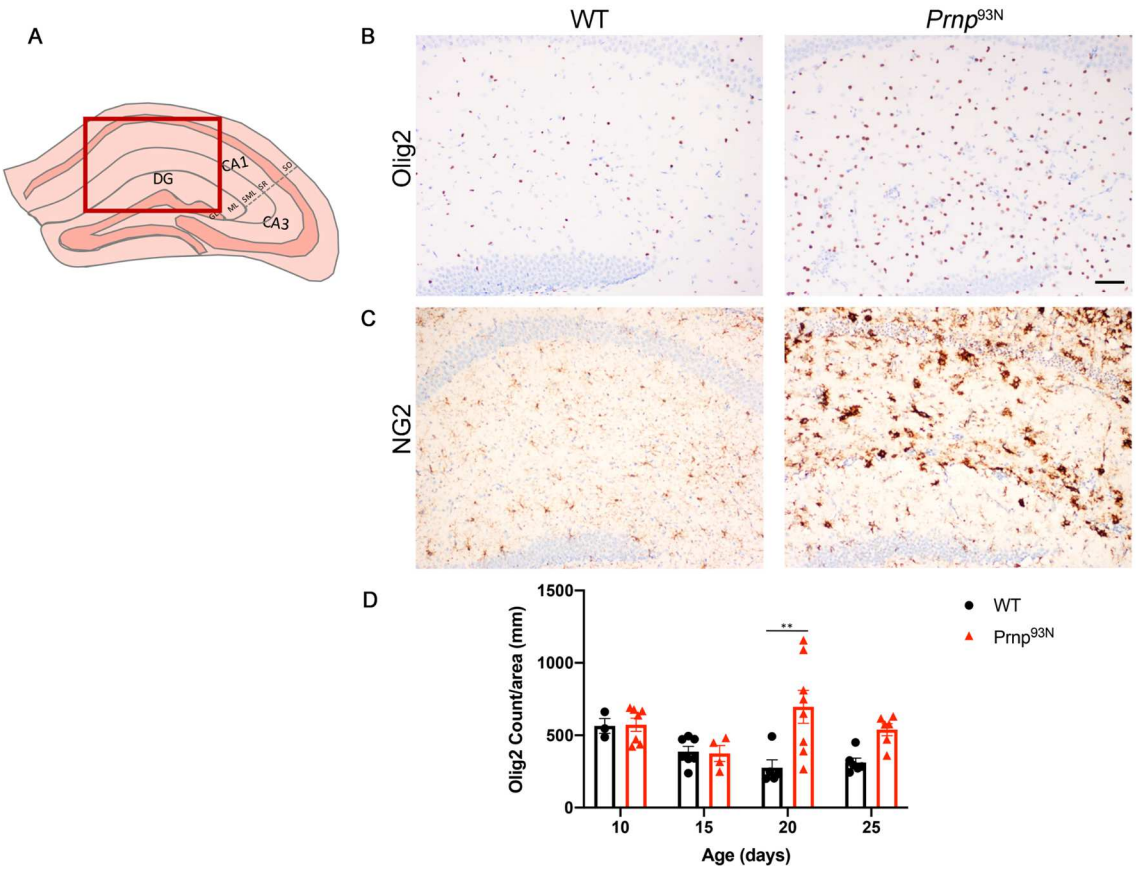

Figure 5. Olig2 and NG2 stain of p25 *Prnp*^{93N} brains. **(A)** Hippocampal diagram of the exact region the following images were taken. **(B)** Olig2 stain of p20 WT and *Prnp*^{93N} hippocampi reveal striking increase of oligodendrocyte numbers in *Prnp*^{93N} hippocampi. Scale bar=200µm. **(C)** NG2 stain of p25 WT and *Prnp*^{93N} hippocampi reveal increase in oligodendrocyte precursor cells in the SR and SML layer of the hippocampus. **(D)** TissueStudio™ quantification of Olig2 reveals significantly greater oligodendrocyte count in *Prnp*^{93N} hippocampi compared to WT at p20, consistent with histology. Statistical comparisons of WT and *Prnp*^{93N} hippocampi were performed by ordinary two-way ANOVA with post-hoc Tukey test (**= $p<0.002$).

To next assess the oligodendrocytes and OPCs, *Prnp*^{93N} and WT brains were immunolabeled for Olig2 and NG2. At p20, Olig2 revealed more oligodendrocytes in *Prnp*^{93N} hippocampus compared to WT hippocampus (Fig. 5D). p20 Olig2 quantification is consistent with histologic findings of greater number of oligodendrocytes in the SR, SML, and ML of the hippocampus (Fig. 5B). There were no significant differences in Olig2 staining in cerebral cortex or thalamus. NG2 staining of *Prnp*^{93N} hippocampi reveal a striking increase in OPCs in *Prnp*^{93N} hippocampi in the stratum radiatum and stratum laculosum moleculare layers compared to WT (Fig. 5C). Together, this suggests that the

increase in oligodendrocyte numbers in *Prnp*^{93N} hippocampi starting at p20 may be due to the increased migration of OPCs after oligodendrocyte insult.

GFAP, A Marker for Astrocytes

Developmental Astrocytes

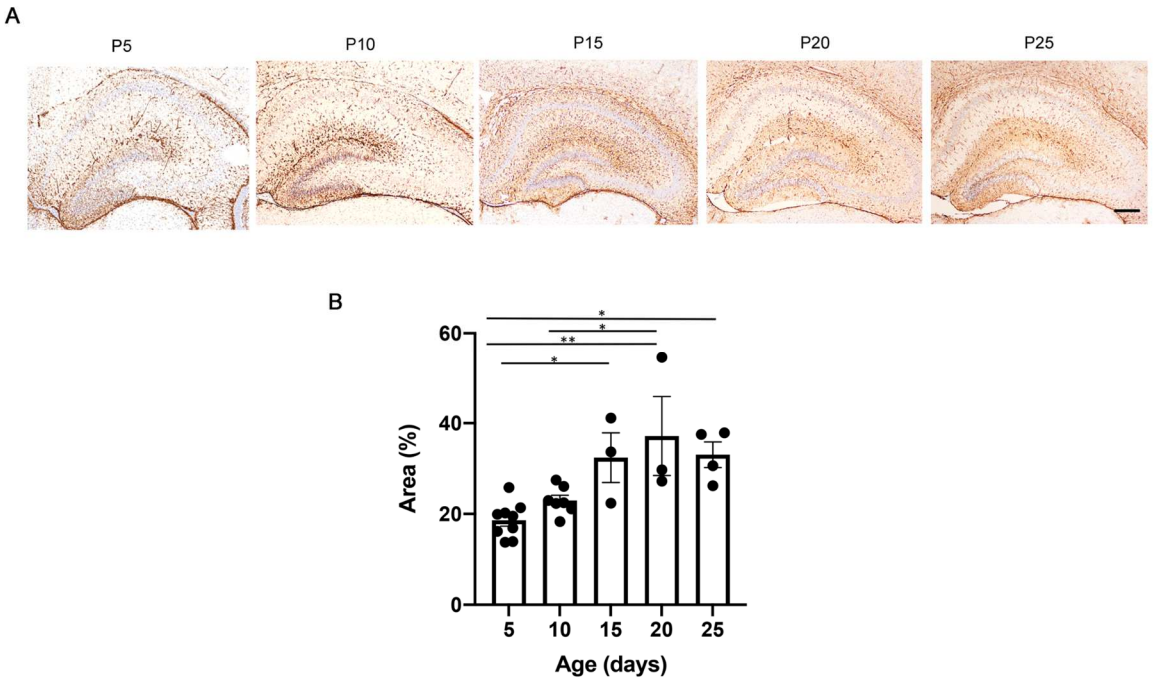

Figure 6. Developmental astrocytes. **(A)** WT mice hippocampi were quantified for GFAP area from p5 to p25. Scale bar=500µm. **(B)** All data are mean + SEM. Statistical comparisons between WT hippocampus among different time were performed by ordinary one-way ANOVA with post-hoc Tukey test (*= $p<0.033$; **= $p<0.002$).

To study the pathology of astrocytes, WT hippocampi were stained with GFAP to assess astrocyte development from p5 to p25 (Fig. 6A). Significant increase in GFAP area was found from p5 to p15 (Fig. 6B), suggesting astrocytes develop their peripheral processes from p5 to p10 and are fully mature starting at p15.

Astrocyte Activation States

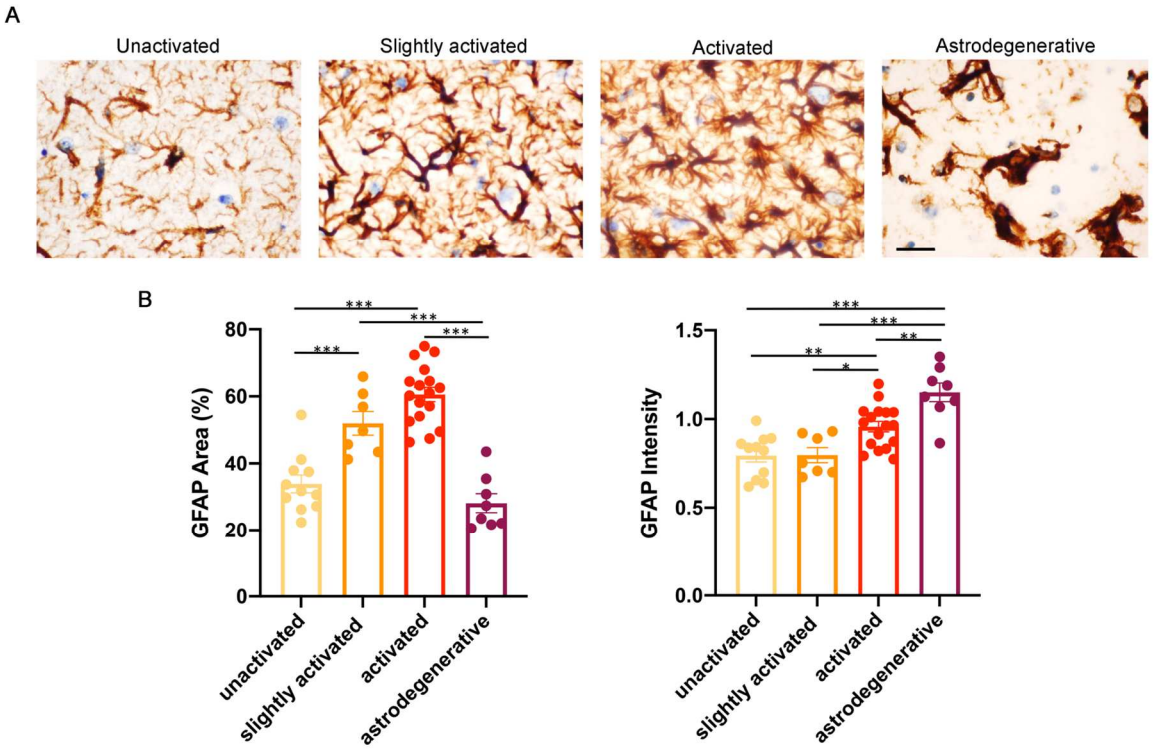

Figure 7. Astrocyte activation states. *Prnp*^{93N} mice hippocampi were categorized by astrocyte morphologies: unactivated, slightly activated, activated, and astrodegenerative. Astrocyte morphologies range from the lease severe (unactivated) to most severe (astrodegenerative). **(A)** Images of different *Prnp*^{93N} hippocampal astrocyte morphologies. Scale bar=20.0µm. **(B)** Hippocampal GFAP area and intensity were quantified by TissueStudio™. All data are mean + SEM. Statistical comparisons among the different astrocyte morphologies were performed by ordinary one-way ANOVA with post-hoc Tukey test (*= p<0.033; **= p<0.002; ***=p<0.001).

Initially, GFAP intensity and area were quantified for WT and *Prnp*^{93N} brain regions: hippocampus, cerebral cortex, and thalamus at timepoints p10, p15, p20, and p25. No significant differences were found comparing GFAP of WT and *Prnp*^{93N} mice brains (Fig. 8C). We then categorized hippocampal astrocytes by the following morphologies: unactivated, slightly activated, activated, and astrodegenerative (Fig. 7A). Unactivated astrocytes have small cell bodies with highly branched, thin distal processes. Moderately activated astrocytes exhibit slight cell body swelling with moderately thickened distal processes. Activated astrocytes have intense cell body swelling and shortened, thickened processes. Degenerative astrocytes are characterized by loss of astrocyte numbers and astrocytic distal processes. To test whether the TissueStudio™ software captures astrocyte morphological differences, GFAP intensity and area were assessed for each morphologic subtype. There were significant

differences in GFAP intensity and area among the four astrocyte morphologies. Activated astrocytes have significantly greater GFAP area compared to unactivated and greater GFAP intensity compared to unactivated and slightly activated. Astrodegenerative morphology has significantly less GFAP area compared to slightly activated and activated, and significantly greater GFAP intensity compared to all the other astrocyte subtypes (Fig. 7B). Astrocyte activation is characterized by increased GFAP expression and proliferation (Brahmachari et al,. 2006). GFAP intensity data suggests astrocyte activation ranges from least severe (unactivated) to most severe (astrodegenerative).

GFAP Timecourse: Astrocytes in *Prnp*^{93N} Hippocampus

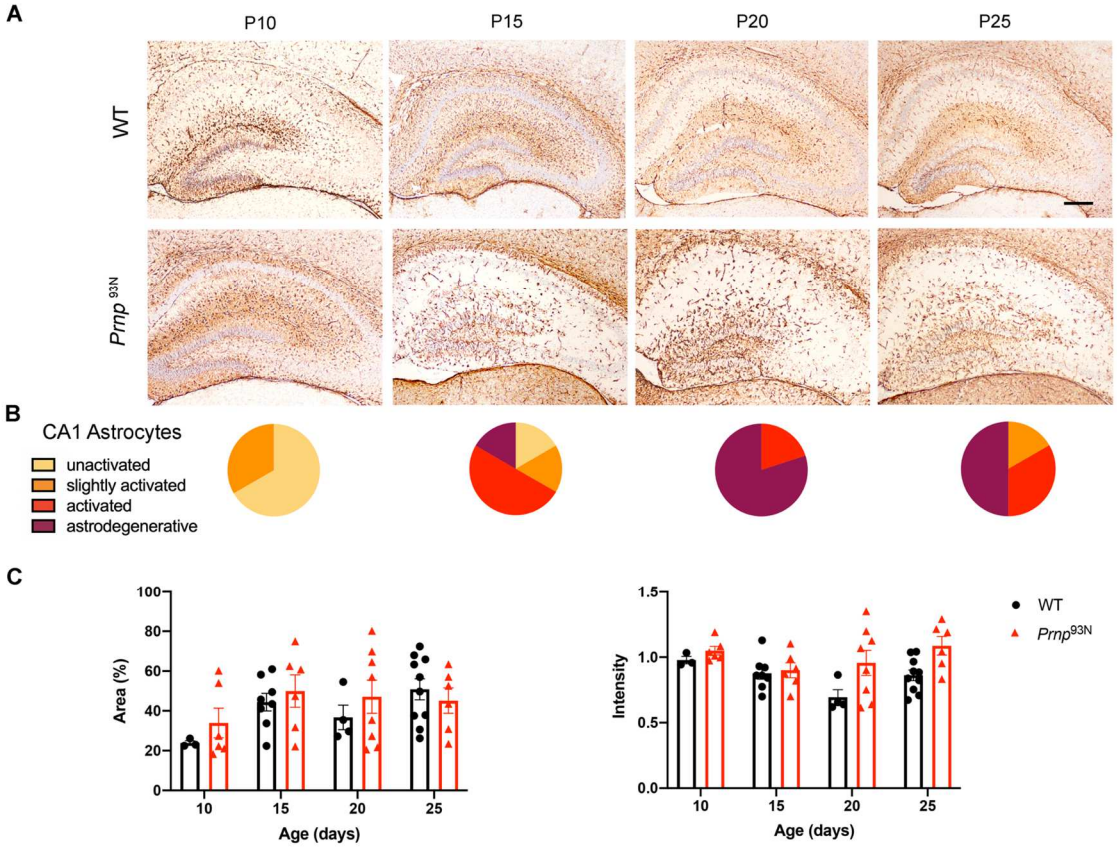

Figure 8. GFAP timecourse study: hippocampus. **(A)** GFAP immunolabeling of WT and *Prnp*^{93N} hippocampi across timepoints p10 to p25. Scale bar=500µm. **(B)** *Prnp*^{93N} CA1 hippocampal astrocytes were categorized by morphologies: unactivated, slightly activated, activated, and astrodegenerative. Pie charts at each timepoint reveal total number of *Prnp*^{93N} hippocampi with CA1 astrocytes exhibiting one type of morphology. **(C)** Hippocampal GFAP area and intensity were quantified by TissueStudio^{TM}. Statistical comparisons of WT and *Prnp*^{93N} mice were performed by ordinary two-way ANOVA with post-hoc Tukey test ($p>0.05$).

Along with SE and neurodegeneration observed in the terminal hippocampus, *Prnp*^{93N} hippocampi also exhibited extreme astrogliosis. To determine timeline of gliosis in *Prnp*^{93N} hippocampi, GFAP was quantified at p10, p15, p20, and p25 timepoints. Though there is a trend of increased GFAP area and intensity in *Prnp*^{93N} hippocampi at p20, no significant differences were found between WT and *Prnp*^{93N}(Fig. 8C). Insignificant data may be due to varying activated astrocyte morphologies seen at each timepoint. At p10, two of six *Prnp*^{93N} mice exhibited activated astrocytes in the CA1 region of the hippocampus and four of six mice exhibited unactivated astrocytes (Fig. 8B). At p15, one of six mice exhibited unactivated, one exhibited slightly activated, three exhibited activated, and one exhibited astrodegenerative phenotype. At p20, of five *Prnp*^{93N} mice, one exhibited activated

phenotype and four exhibited astrodegenerative phenotype. At p25, of six *Prnp*^{93N} mice, one exhibited slightly activated, two exhibited activated, and three exhibited astrodegenerative phenotype. This data suggests *Prnp*^{93N} hippocampal astrocyte activation begins at p10 and astrocytes assume more severe activation states as disease course progresses.

GFAP Timecourse: Astrocytes in *Prnp*^{93N} Cerebral Cortex

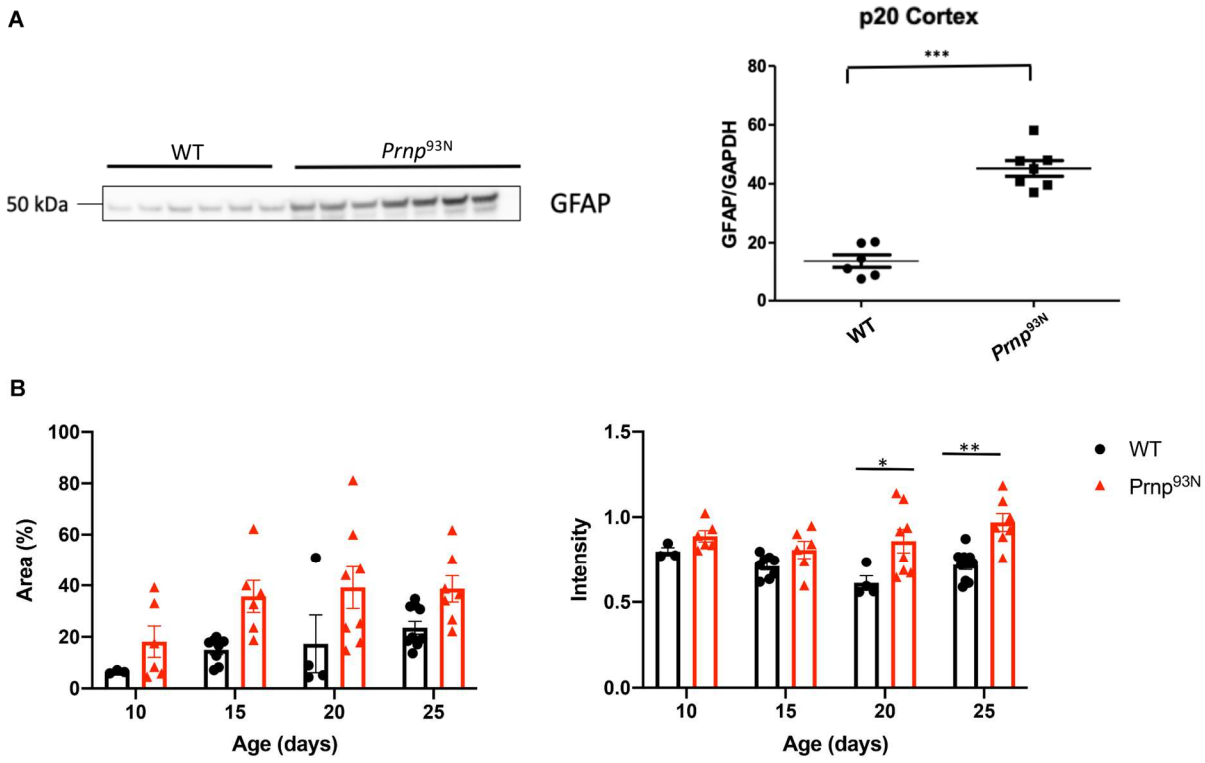

Figure 9. GFAP timecourse study: cerebral cortex. GFAP in cerebral cortex of WT and *Prnp*^{93N} mice were analyzed. **(A)** Western blot probing for GFAP was performed on p20 WT and *Prnp*^{93N} cortices. Western blot analysis reveals significantly greater GFAP expression in p20 *Prnp*^{93N} cortex compared to that of WT. Unpaired student t-test was performed ($p<0.001$). **(B)** GFAP area and intensity of WT and *Prnp*^{93N} mice cortex were analyzed by TissueStudio™. All data are mean + SEM. Statistical comparison of WT and *Prnp*^{93N} was performed by ordinary two-way ANOVA test with post-hoc Tukey test (*= $p<0.033$; **= $p<0.002$).

The next brain region of interest is the cerebral cortex. GFAP staining of WT and *Prnp*^{93N} cortex revealed a significantly greater GFAP intensity in *Prnp*^{93N} cortex compared to WT at p20 and p25 (Fig. 9B). To confirm accuracy of GFAP quantification, western blot probing for GFAP was performed on p20 WT and *Prnp*^{93N} cortices

(Fig. 9A). Western blot analysis revealed significantly higher GFAP expression in *Prnp*^{93N} cortex compared to WT, consistent with GFAP intensity quantification p20. This data suggests *Prnp*^{93N} cortical astrocytes are activated at p20 and p25.

GFAP Timecourse: Astrocytes in *Prnp*^{93N} Thalamus

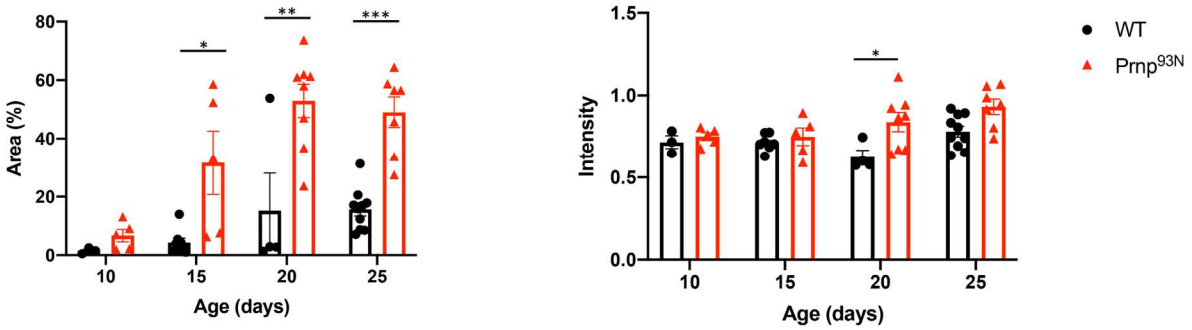

Figure 10. GFAP timecourse study: thalamus. GFAP area and intensity in thalamus of WT and *Prnp*^{93N} mice were analyzed by TissueStudio™. All data are mean + SEM. Statistical comparison of WT and *Prnp*^{93N} cortices was performed by ordinary two-way ANOVA test with post-hoc Tukey test (*= $p<0.033$; **= $p<0.002$; ***=$p<0.001$).

Astrogliosis was also measured in the thalamus. At p15, p20, and p25, *Prnp*^{93N} thalamus have significantly greater GFAP area compared to that of WT. At p20, there is also significantly greater GFAP intensity in *Prnp*^{93N} thalamus compared to that of WT (Fig. 10). This data suggests *Prnp*^{93N} thalamic astrocytes are activated starting at p15.

Iba-1, A Marker for Microglia

Developmental Microglia

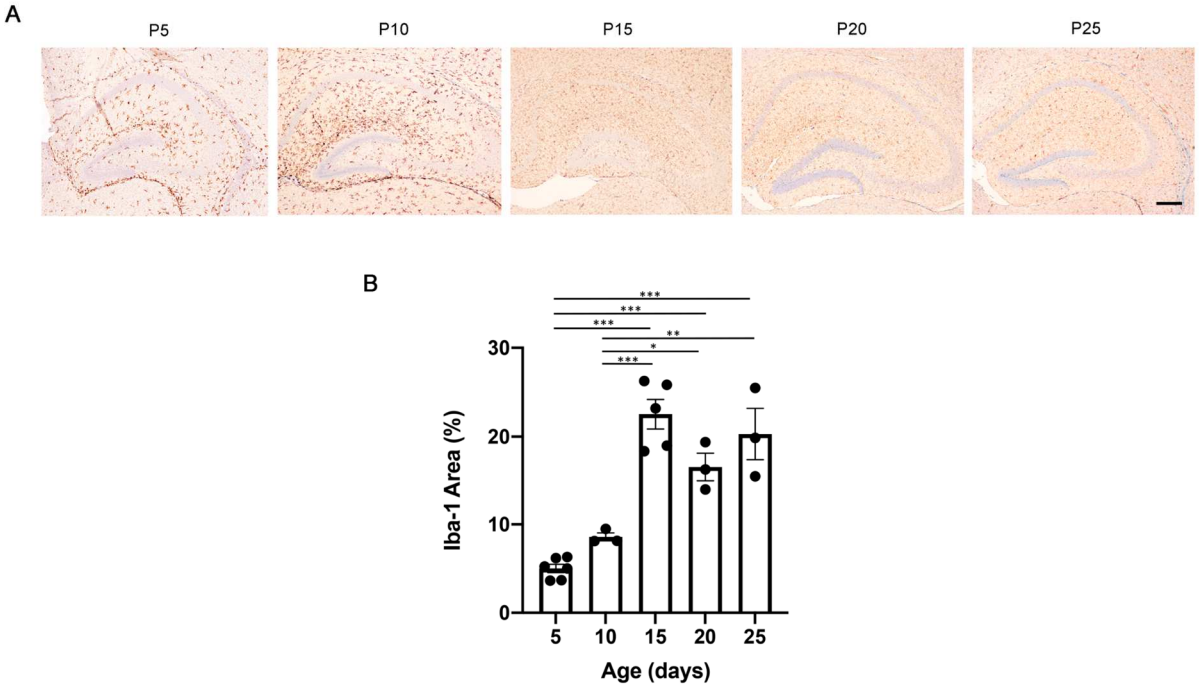

Figure 11. Developmental microglia. **(A)** WT mice hippocampi were quantified for Iba1 area from p5 to p25. Scale bar=500µm. **(B)** All data are mean + SEM. Statistical comparisons between WT hippocampus among different time were performed by ordinary one-way ANOVA with post-hoc Tukey test (*= $p<0.033$; **= $p<0.002$; ***=$p<0.001$).

Another important glial cell studied is the microglia. To assess microglial pathology early in disease, WT microglial development must be understood. WT hippocampi were stained with Iba1 to assess normal microglial development at timepoints p5, p10, p15, p20, and p25 (Fig. 11A). Significant increase in Iba1 area was found from p5 to p15 (Fig. 11B). This suggests microglia begin developing peripheral processes from p5 to p10, and are fully mature starting at p15.

Microglia Activation States

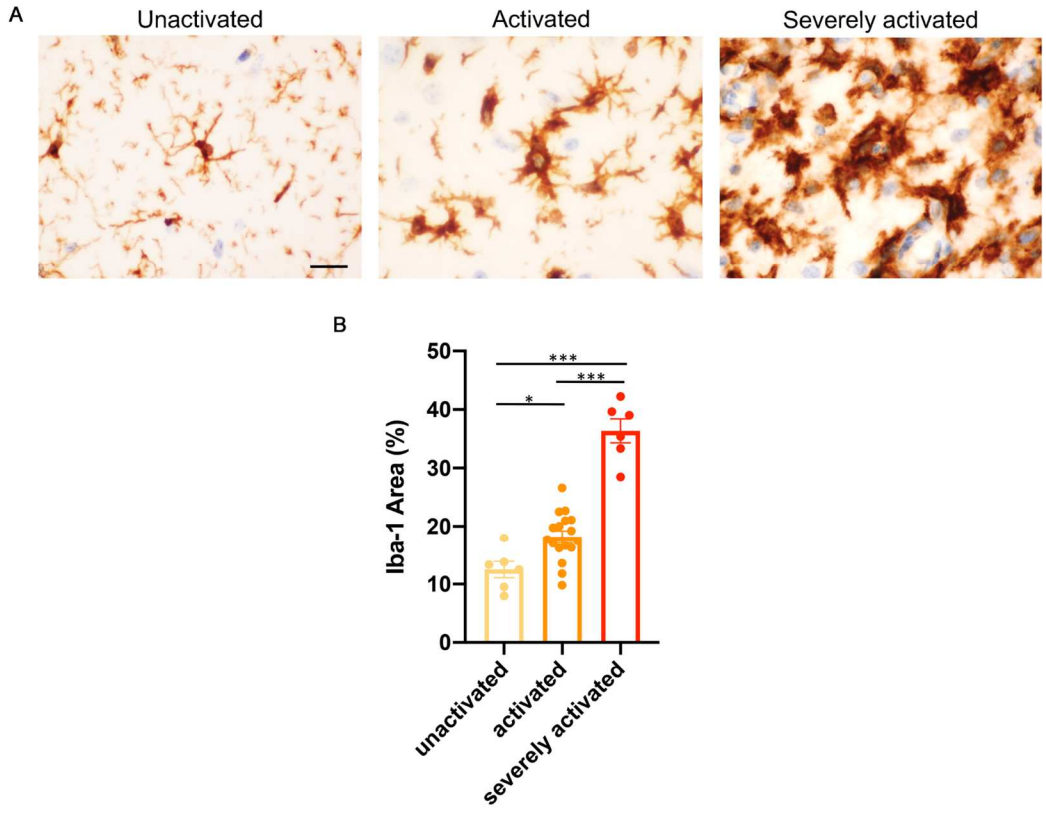

Figure 12. Activated microglial states. *Prnp*^{93N} hippocampal microglia were categorized by morphologies: unactivated, activated, and severely activated. Microglial morphologies range from the lease severe (unactivated) to most severe (severely activated). **(A)** *Prnp*^{93N} hippocampal microglia images of each morphology. Scale bar=20.0µm. **(B)** Iba-1 area were quantified by TissueStudio™. All data are mean + SEM. Statistical comparisons among the different microglial morphologies were performed by ordinary one-way ANOVA with post-hoc Tukey test (*= $p<0.033$; ***=$p<0.001$).

Similar to astrocytes, microglia can also take on various activation states: unactivated, activated, and severely activated. Unactivated microglia have small cell bodies with highly branched, thin processes. Activated microglia exhibit swelling of cell body with moderately thickened distal processes. Severely activated microglia morphology is characterized by severe cell body swelling and short, thickened processes (Fig. 12A). To next test whether TissueStudio™ captures microglial morphological differences, Iba1 area was assessed for each morphologic subtype. There were significant differences in Iba1 area among the three microglia morphologies. Unactivated microglia have the lowest Iba1 area, followed by the activated. Severely activated have the greatest Iba1 area (Fig. 12B).

Iba1 Timecourse: Microglia in Prnp^{93N} Hippocampus

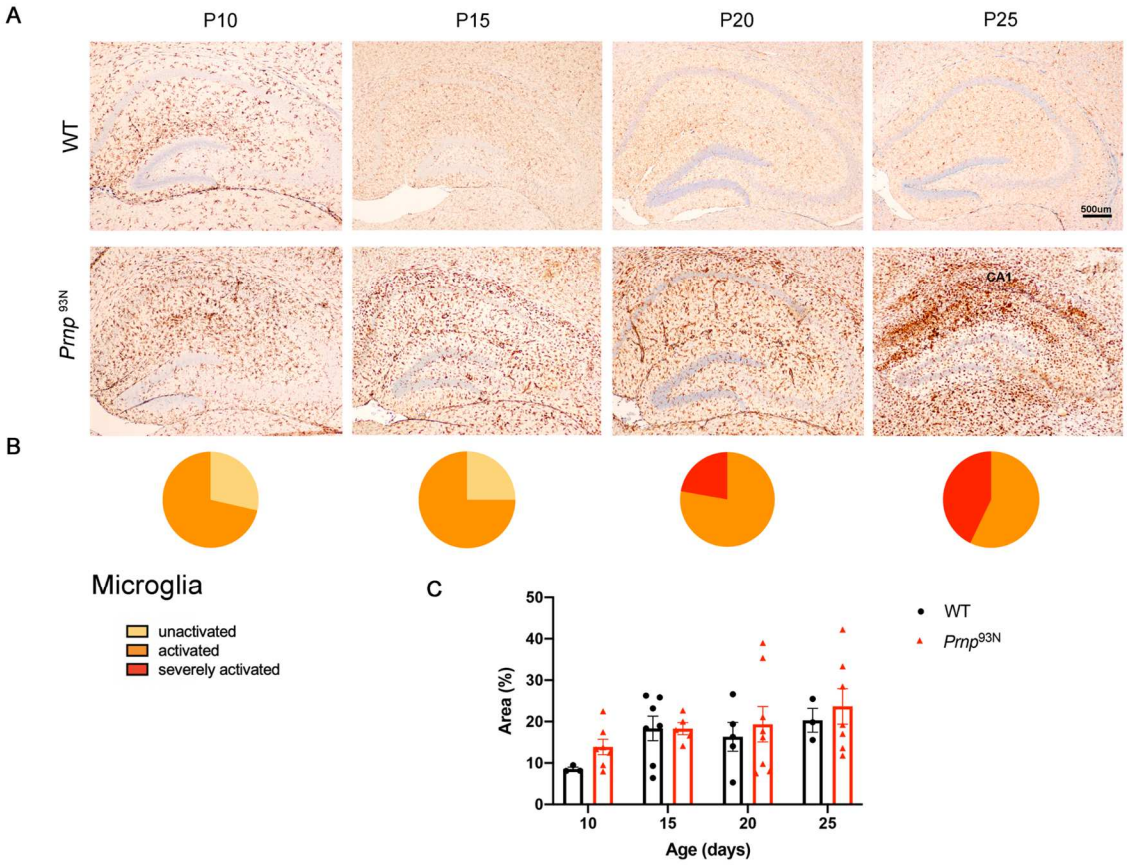

Figure 13. Iba1 timecourse: hippocampus. **(A)** Iba1 immunolabeling of WT and *Prnp*^{93N} hippocampi across timepoints p10 to p25. Scale bar=500µm. **(B)** *Prnp*^{93N} CA1 hippocampal microglia were categorized by morphologies: unactivated, activated, and severely activated. Pie charts at each timepoint reveal total number of *Prnp*^{93N} hippocampi containing CA1 microglia of one activated morphology. **(C)** Hippocampal Iba1 area and intensity were quantified by TissueStudio^{TM}. Statistical comparisons of WT and *Prnp*^{93N} mice were performed by ordinary two-way ANOVA with post-hoc Tukey test ($p>0.05$).

Initial assessment of terminal *Prnp*^{93N} hippocampus also revealed extreme microgliosis in the CA1 region of the hippocampus. To determine timeline of microgliosis in *Prnp*^{93N} hippocampi, Iba1 stains were performed and Iba1 area was quantified at p10, p15, p20, and p25 timepoints (Fig. 13A). Though not significant, Iba-1 area trends higher in the p20 and p25 *Prnp*^{93N} hippocampus compared to WT (Fig. 13C). At each timepoint, a number of *Prnp*^{93N} mice exhibited CA1 microglia of one specific morphology. At p10, of seven *Prnp*^{93N} hippocampi, two exhibited unactivated CA1 microglia and five exhibited activated microglia. At p15, of four *Prnp*^{93N} hippocampi, one exhibited unactivated microglia and three exhibited activated microglia. At p20, of seven *Prnp*^{93N} hippocampi seven exhibited activated microglia and two exhibited severely activated microglial. At p25, four of seven mice

exhibited activated and three exhibited severely activated CA1 microglia (Fig. 13B). This data suggests hippocampal microglia begin activation at p10 and assume more severe activation states as disease progresses. No significant differences in Iba1 area were found for cerebral cortex and thalamus between WT and *Prnp*^{93N}.

Lamp1 in *Prnp*^{93N} Hippocampus

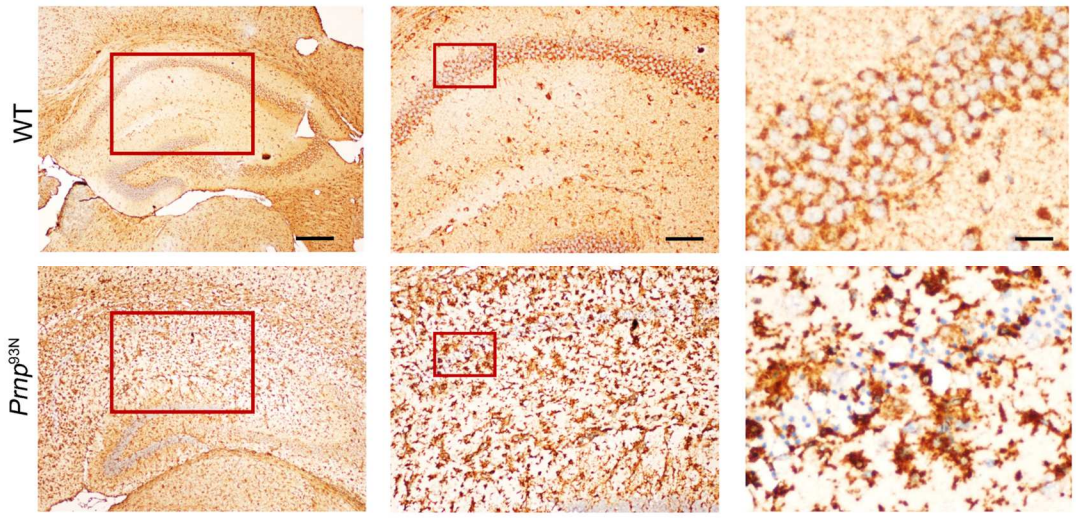

Figure 14. Lamp1 in *Prnp*^{93N} Hippocampus. p25 WT and *Prnp*^{93N} hippocampi stained with Lamp1 reveal striking differences in lysosome distribution in cells. From left to right, scale bars= 500, 200, and 50.0µm.

Since severe microgliosis was noted in *Prnp*^{93N} hippocampi at p25. Lamp1, marker for degradative autophagy-lysosomal organelles was assessed in p25 *Prnp*^{93N} hippocampi. In the WT hippocampus, Lamp1 is expressed ubiquitously with very light stain. In contrast, Lamp1 in the p25 *Prnp*^{93N} hippocampus is highly expressed in cell bodies with great intensity (Fig. 14). The *Prnp*^{93N} hippocampus may experience an upregulation of lysosomes or an accumulation of lysosomes in cell bodies.

Summary of *Prnp*^{93N} Pathology: Gliosis

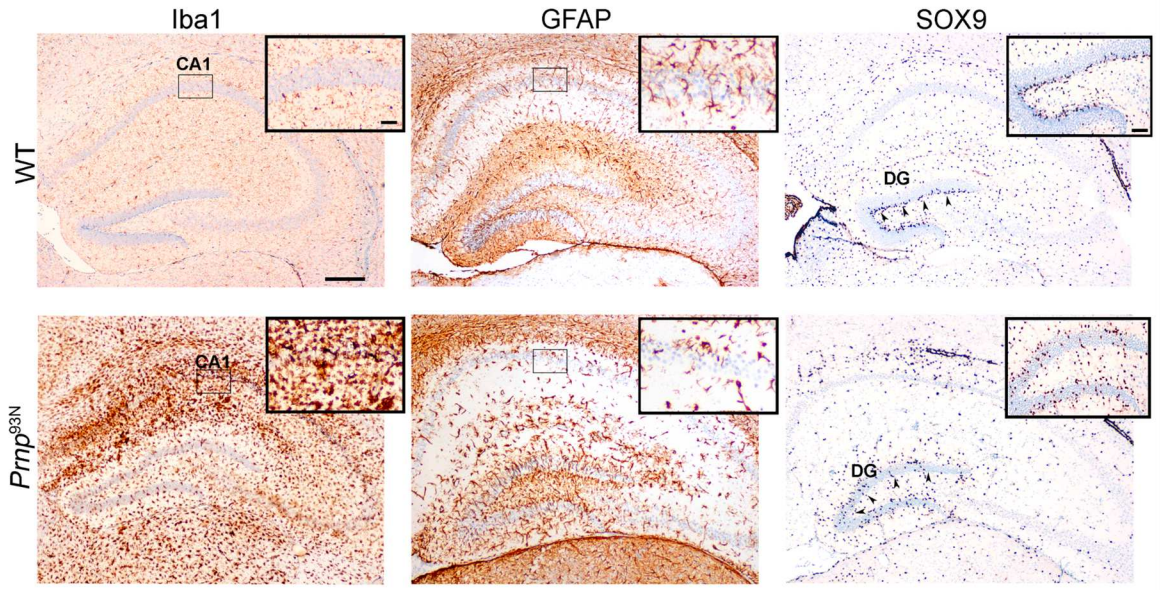

Figure 15. Summary of *Prnp*^{93N} pathology: Gliosis. p25 WT and *Prnp*^{93N} hippocampi stained for microglia (Iba1) and astrocytes (GFAP and SOX9). Scale bar= 500µm. For Iba1 and GFAP insets, scale bar= 50.0µm. For SOX9 insets, scale bar=200µm. Arrows are pointing to neural progenitor cells in the dentate gyrus.

Summary of *Prnp*^{93N} Pathology: Neuronal Loss and Oligodendrocyte Pathology

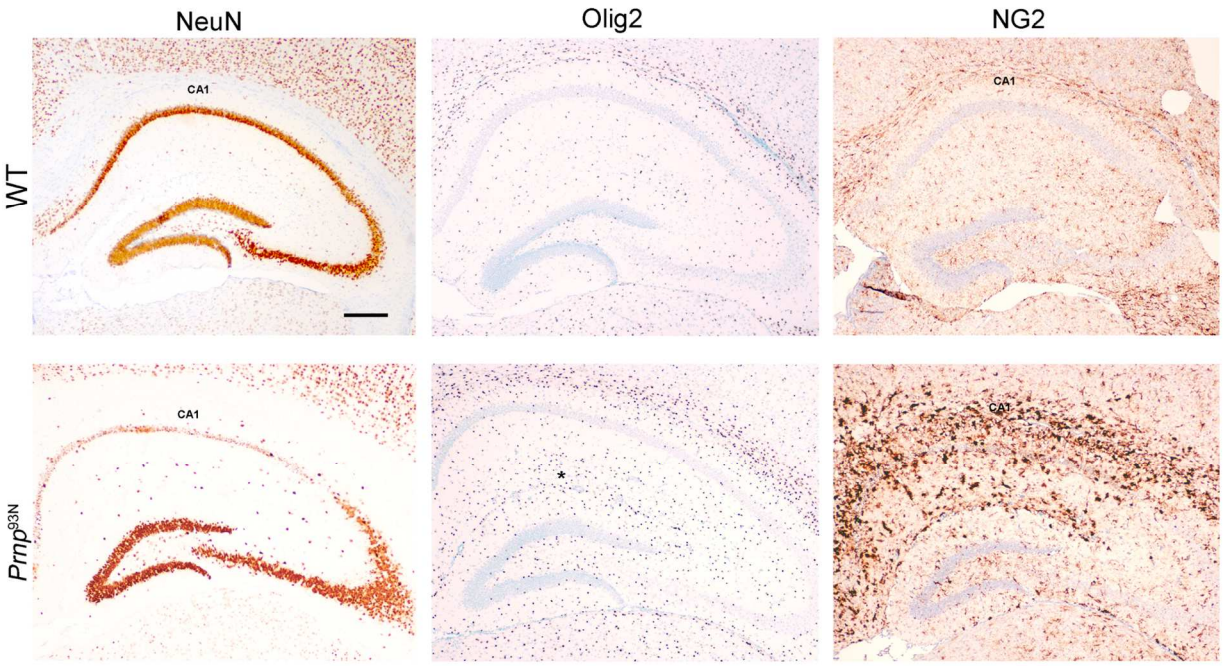

Figure 16. Summary of *Prnp*^{93N} pathology: neuronal loss and oligodendrocyte pathology. p25 WT and *Prnp*^{93N} hippocampi stained for neurons (NeuN), oligodendrocytes (Olig2), and OPCs (NG2). Scale bar= 500µm. *Prnp*^{93N} hippocampal layers: stratum radiatum, stratum laculosum moleculare and molecular layer of dentate gyrus exhibit greater oligodendrocyte numbers compared to that of WT (asterisk).

Prnp^{93N} Pathology Timeline

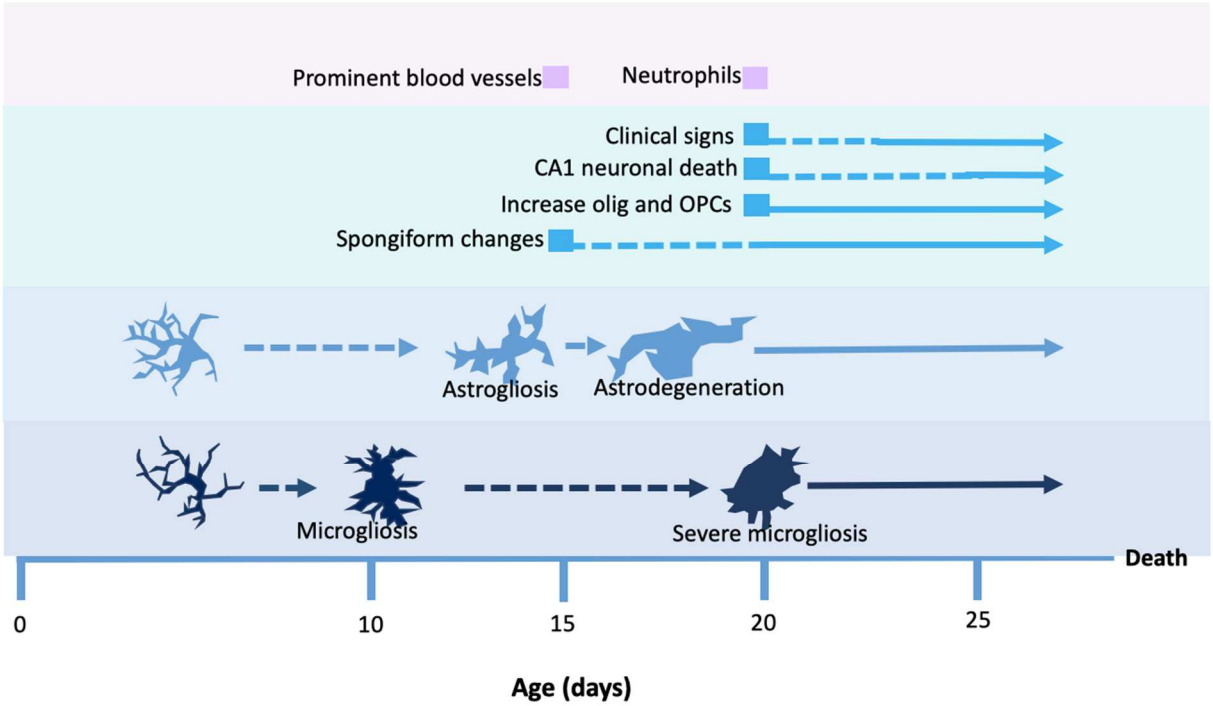

Figure 17. Summary diagram of *Prnp*^{93N} hippocampus pathology. Dashed lines represent the start of hippocampal pathology, with some mice hippocampi beginning to exhibit pathology. Solid lines represent when most hippocampi exhibit pathology.

DISCUSSION

In this study, we have characterized the neuropathology of the 93N knock-in model of neurodegeneration. The hippocampus was the most severely affected brain region. By conducting a longitudinal study, we now understand when cellular pathologies arise and can address the question of whether the 93N mice experience neurodevelopmental or neurodegenerative disease as a result of this PrP^{C} mutation.

The *Prnp*^{93N} mice show a striking neuronal loss in the CA1 region of the hippocampus as early as p20 possibly because they express more NMDA NR2 subunits than other CA regions (Butler et al., 2010) (Anand and Dhikav, 2012). Neuronal death and inflammation may be further exacerbated by neutrophils in the brain at p20. To understand the mechanism of neuronal death, cleaved caspase-3 stain was performed to assess apoptosis. Minimal cleaved caspase-3 staining of *Prnp*^{93N} hippocampi suggests the main mechanism of neuronal loss may be necrosis, which is consistent with electron microscopy images of *Prnp*^{93N} CA1 neurons (Unpublished data, 2021).

SE was seen in *Prnp*^{93N} hippocampus and thalamus as early as p15 when compared to WT. Interestingly, this may be due to the additional N-terminal glycan in PrP^{C} resulting in toxic signaling and causing SE in the absence of aggregates. When comparing *Prnp*^{93N} SE to mock-inoculated and prion (22L)-inoculated, there were no significant differences between hippocampus scores. This suggests that the *Prnp*^{93N} mice may be a good model for prion disease as they exhibit SE as early as p15.

Astrocyte pathology arises at p10, when *Prnp*^{93N} mice show the first signs of slightly activated astrocytes in the CA1 region of the hippocampus. By p20 and p25, *Prnp*^{93N} hippocampi exhibit activated and astrodegenerative morphologies. Developing astrocytes may be affected by the pro-inflammatory cytokines secreted by activated microglia. At p15, astrocytes are fully developed with mature PAPs. Activated astrocytes have been noted in many neurodegenerative diseases including prion disease and Alzheimer's disease and can play neuroprotective roles including secretion of neurotrophic factors. Another neuroprotective role includes promoting remyelination after oligodendrocyte damage (McTigue et al., 2008) (Wang et al., 2017). The activated astrocytes may be increasing the oligodendrocyte numbers and OPC migration into the hippocampus at p20 and p25. Neurotoxic roles including secretion of inflammatory factors (Kajihara et al., 2001). Activated astrocytes may also be responsible for the presence of neutrophils in the hippocampus and thalamus, as they can secrete chemokines such as CXCL1 to recruit neutrophil infiltration into the brain (Michael et al., 2020). These recruited neutrophils can release inflammatory factors that can induce further neuronal damage (Kanashiro et al., 2020).

Astrodegenerative phenotypes have been observed in neuropsychiatric disorders including schizophrenia, major depressive disorder, and Alzheimer's disease. They have been associated with impairment of glutamate homeostasis (Verkhratsky et al, 2019) (Frost et al., 2017). As astrocytic degeneration occurs, astrocytes lose their PAPs, which contain essential membrane proteins including GLT1/GLAST, important for regulating glutamate homeostasis. Thus, astrocytic degeneration may contribute to glutamate-mediated excitotoxicity responsible for the CA1 neuronal death seen at p20. Another important function of astrocytes includes preservation of the BBB by astrocytic perivascular endfeet. The loss of peripheral processes and perivascular endfeet in the degenerative astrocytes may contribute to diminished BBB integrity and result in the presence of prominent endothelial cells in the blood vessels at p15 and subsequent infiltration of neutrophils at p20.

We found that microglia increase in number and in peripheral processes from p5 and p10 up until p15 in the WT mice, consistent with studies that show microglia reach peak numbers in the brain at around p14 (Lenz et al., 2018) (Kim et al., 2015) (Nikodemova et al., 2014). Interestingly, p10 *Prnp*^{93N} hippocampi display activated microglia in the CA1 region. By p20, *Prnp*^{93N} brains begin displaying severely activated microglia in the CA1 hippocampal region. Activated microglia contribute to pathology in many neurodegenerative diseases by secreting of pro-inflammatory cytokines including IL-1, IL-6, and TNF-alpha (Smith et al., 2012). These inflammatory cytokines could be acting on astrocytes to trigger their activation starting at p10 and increasing severity of their activation state at p15 and onward. Pro-inflammatory cytokines can also cause CA1 neuronal loss as they are known to be toxic to neurons and other glial cells (Smith et al., 2012). Furthermore, neuronal death in the CA1 region may activate microglia to phagocytose cellular debris. Interestingly, high intensity Lamp1 stain within cells in the *Prnp*^{93N} hippocampi suggests impairment of endolysosomal trafficking or autophagy pathways.

We have developed a model explaining *Prnp*^{93N} mice pathology in the hippocampus. Starting at p10, microglia experience early developmental changes due to its expression of mutated PrP^{C}. These activated microglia secrete pro-inflammatory cytokines including IL-1, IL-6, and TNF-alpha that begin to activate astrocytes at p10. Slightly activated astrocytes at p10 can also be activated in response to their expression of mutated PrP^{C}. Then, at p15, the first astrodegenerative morphology arises. Prominent blood vessels first appear at p15 due to astrodegeneration and loss astrocytic endfeet. Astrodegeneration also contributes to an extracellular environment of excessive glutamate at this point. Spongiform changes are also seen starting at p15 due to PrP^{C} neurotoxic signaling. Starting at p20, the *Prnp*^{93N} mice show the first clinical signs, including kyphosis, hindleg clasp, and gait

abnormalities. Histologically, p20 is coincident with the first observations of CA1 neuronal loss, possibly due to loss of glutamate regulation by astrocytes and continual secretion of pro-inflammatory cytokines by activated microglia. At p20, neutrophil recruitment by CXCL1 from activated astrocyte also exacerbates neuronal damage. Severely activated microglia are mobilize to CA1 region to phagocytose dying neurons at p20. At p20, oligodendrocyte also experience insult from glutamate-mediated toxicity and numbers oligodendrocyte numbers increase from remyelination and OPC migration aided by astrocytes.

Together these data suggest that the *Prnp*^{93N} mice have a developmental disease as well as a neurodegenerative disease. *Prnp*^{93N} mice experience a developmental disease, as differences were observed in microglial and astrocyte development as early as p10, while neurodegeneration does not occur until p20. This suggests there is a developmental pathology in *Prnp*^{93N} glial cells that contribute to early neurodegeneration and rapid death at p25 and p30.

Glutamate-mediated toxicity, a possible mechanism

Toxic glutamate levels are hypothesized to arise from degenerative astrocytes as early as p15 as a result of astrocytes' loss of ability to regulate glutamate homeostasis. This excess in extracellular glutamate levels could activate NMDA receptors to cause excessive calcium influx that may result in toxicity. Seizures in *Prnp*^{93N} mice also support the hypothesis of glutamate mediated toxicity in the mice.

Other studies in our lab have assessed glutamate response in cortical *Prnp*^{93N} neurons in *vitro* and have found an increase in susceptibility of glutamate-mediated excitotoxicity. This suggests that *Prnp*^{93N} cells may inherently be more susceptible to glutamate-mediated excitotoxicity. Furthermore, toxic amounts of glutamate in the extracellular environment in addition to their high susceptibility to glutamate-mediated excitotoxicity may cause rapid neurodegeneration in the *Prnp*^{93N} mice.

Another hypothesis directly involves activation of the NMDA receptors. Studies have shown that the octapeptide repeat domain is necessary for ion conductance as its deletion abolishes neurotoxicity (Solomon et al., 2011) (Wu et al., 2017). The *Prnp*^{93N} mouse model has a third glycan inserted in the N-terminal, in close proximity to the octapeptide repeat domain. This large glycan can sterically inhibit the interaction between the C-terminal regulator and the octapeptide domain. This inhibition of N-terminal regulation can result the chronic neurotoxic signaling by continuous activation of NMDA glutamate receptors, resulting in significant increase in calcium ion

influx in neurons, especially CA1 pyramidal neurons. This excessive calcium influx can activate intracellular pathways such as the p38 MAPK pathway to cause dendritic spine and synapse damage, and other neuropathological effects also see in prion disease (Le et al., 2019).

In support of the *Prnp*^{93N} toxic signaling via chronic activation of NMDA receptors, other lab members have found that the *Prnp*^{93N} cortical neurons *in vitro* exhibit dendritic beading, an excitotoxic phenotype that is rescued by application of NMDA receptor antagonist, MK801.

Summary and Future Studies

This study provides the first histology descriptions of the novel *Prnp*^{93N} mouse model, in which one single nucleotide mutation results in the addition of a third glycan in the N-terminal domain. Such disruption in the N-terminal domain results in mice with extreme alterations in glial cells starting at p10, neurodegeneration at p20, and mice terminal as early as p25. From this longitudinal study, we now know the sequence of histopathological events in the *Prnp*^{93N} mice brains. From here, we can further elucidate how mutated PrP^{C} expression affects glial cells and determine the mechanism of PrP^{C} toxic signaling in neurodegeneration.

Prnp^{93N} mice experience neuronal loss specifically in the CA1 region of the hippocampus. Cleaved caspase-3 does not support apoptosis as the main mechanism of cell death seen in *Prnp*^{93N} mice. Furthermore, high magnification of the *Prnp*^{93N} CA1 region reveals much smaller, condensed nuclei, consistent with necrosis. To confirm cell death by necrosis, an IHC stain for necrotic cell markers including ALT, FK18, miR-122, and HMGB1 (Yang et al., 2014) could be performed.

To determine whether *Prnp*^{93N} neurons are suffering from glutamate-induced neurotoxicity, extracellular glutamate can be measured in p10 neurons, before we see astrodegenerative astrocytes, and after p20, when all hippocampal astrocytes in CA1 region begin exhibiting activated and astrodegenerative phenotypes. EAAT2 receptor levels, excitatory amino acid transporter 2, to determine when glutamate homeostasis is disrupted and assess whether excess glutamate is due to astrocytic loss of function could be performed. A KI-67 stain, which looks at astrocyte proliferation to see if there is a possible repopulation of astrocytes after astrodegeneration, could be performed.

Since we know now that microglia are activated as early as p10, a timecourse study of microglial inflammatory markers could be performed. Microglial pro-inflammatory markers can include IL-1, IL-6, and TNF-alpha (Smith et

al., 2012). Furthermore, since neutrophils are found in the *Prnp*^{93N} hippocampus and thalamus, it would be interesting to assess possible BBB leakage in *Prnp*^{93N} p20 mice.

Ultimately, the novel *Prnp*^{93N} mouse model could be used to study toxic PrP^{C} signaling and spontaneous neurodegeneration in prion disease, Alzheimer's disease, and other neurodegenerative diseases involving aberrant PrP^{C} signaling. Furthermore, novel therapeutics targeting PrP^{C} signaling could be tested for effectiveness on the *Prnp*^{93N} model, as this model provides a rapid *in vivo* assessment of therapeutics, with obvious results as early as 25 days.

REFERENCES

Anand, K. S., & Dhikav, V. (2012). Hippocampus in health and disease: An overview. *Annals of Indian Academy of Neurology*, *15*(4), 239–246. https://doi.org/10.4103/0972-2327.104323

Barateiro, A., Brites, D., & Fernandes, A. (2016). Oligodendrocyte Development and Myelination in Neurodevelopment: Molecular Mechanisms in Health and Disease. *Current pharmaceutical design*, *22*(6), 656–679. https://doi.org/10.2174/1381612822666151204000636

Bezzi, P., Domercq, M., Brambilla, L., Galli, R., Schols, D., De Clercq, E., Vescovi, A., Bagetta, G., Kollias, G., Meldolesi, J., & Volterra, A. (2001). CXCR4-activated astrocyte glutamate release via TNFalpha: amplification by microglia triggers neurotoxicity. *Nature neuroscience*, *4*(7), 702–710. https://doi.org/10.1038/89490

Black, S. A., Stys, P. K., Zamponi, G. W., & Tsutsui, S. (2014). Cellular prion protein and NMDA receptor modulation: protecting against excitotoxicity. *Frontiers in cell and developmental biology*, *2*, 45. https://doi.org/10.3389/fcell.2014.00045

Brandner, S., Isenmann, S., Raeber, A., Fischer, M., Sailer, A., Kobayashi, Y., Marino, S., Weissmann, C., & Aguzzi, A. (1996). Normal host prion protein necessary for scrapie-induced neurotoxicity. *Nature*, *379*(6563), 339–343. https://doi.org/10.1038/379339a0

Butler, T. R., Self, R. L., Smith, K. J., Sharrett-Field, L. J., Berry, J. N., Littleton, J. M., Pauly, J. R., Mulholland, P. J., & Prendergast, M. A. (2010). Selective vulnerability of hippocampal cornu ammonis 1 pyramidal cells to excitotoxic insult is associated with the expression of polyamine-sensitive N-methyl-D-asparate-type glutamate receptors. *Neuroscience*, *165*(2), 525–534. https://doi.org/10.1016/j.neuroscience.2009.10.018

Chen, W., van der Kamp, M. W., & Daggett, V. (2014). Structural and dynamic properties of the human prion protein. *Biophysical journal*, *106*(5), 1152–1163. https://doi.org/10.1016/j.bpj.2013.12.053

Colonna, M., & Butovsky, O. (2017). Microglia Function in the Central Nervous System During Health and Neurodegeneration. *Annual review of immunology*, *35*, 441–468. https://doi.org/10.1146/annurev-immunol-051116-052358

Datta, M., Staszewski, O., Raschi, E., Frosch, M., Hagemeyer, N., Tay, T. L., Blank, T., Kreutzfeldt, M., Merkler, D., Ziegler-Waldkirch, S., Matthias, P., Meyer-Luehmann, M., & Prinz, M. (2018). Histone Deacetylases 1 and 2 Regulate Microglia Function during Development, Homeostasis, and Neurodegeneration in a Context-Dependent Manner. *Immunity*, *48*(3), 514–529.e6. https://doi.org/10.1016/j.immuni.2018.02.016

Drisaldi, B., Coomaraswamy, J., Mastrangelo, P., Strome, B., Yang, J., Watts, J. C., Chishti, M. A., Marvi, M., Windl, O., Ahrens, R., Major, F., Sy, M. S., Kretzschmar, H., Fraser, P. E., Mount, H. T., & Westaway, D. (2004). Genetic mapping of activity determinants within cellular prion proteins: N-terminal modules in PrPC offset pro-apoptotic activity of the Doppel helix B/B' region. *The Journal of biological chemistry*, *279*(53), 55443–55454. https://doi.org/10.1074/jbc.M404794200

Escartin, C., Galea, E., Lakatos, A., O'Callaghan, J. P., Petzold, G. C., Serrano-Pozo, A., Steinhäuser, C., Volterra, A., Carmignoto, G., Agarwal, A., Allen, N. J., Araque, A., Barbeito, L., Barzilai, A., Bergles, D. E., Bonvento, G., Butt, A. M., Chen, W. T., Cohen-Salmon, M., Cunningham, C., … Verkhratsky, A. (2021). Reactive astrocyte nomenclature, definitions, and future directions. *Nature neuroscience*, *24*(3), 312–325. https://doi.org/10.1038/s41593-020-00783-4

Evans, E. G., Pushie, M. J., Markham, K. A., Lee, H. W., & Millhauser, G. L. (2016). Interaction between Prion Protein's Copper-Bound Octarepeat Domain and a Charged C-Terminal Pocket Suggests a Mechanism for N-Terminal Regulation. *Structure (London, England : 1993)*, *24*(7), 1057–1067. https://doi.org/10.1016/j.str.2016.04.017

Fang, C., Wu, B., Le, N., Imberdis, T., Mercer, R., & Harris, D. A. (2018). Prions activate a p38 MAPK synaptotoxic signaling pathway. *PLoS pathogens*, *14*(9), e1007283. https://doi.org/10.1371/journal.ppat.1007283

Fischer, M., Kaech, S., Wagner, U., Brinkhaus, H., & Matus, A. (2000). Glutamate receptors regulate actin-based plasticity in dendritic spines. *Nature neuroscience*, *3*(9), 887–894. https://doi.org/10.1038/78791

Franklin, R., & Ffrench-Constant, C. (2017). Regenerating CNS myelin - from mechanisms to experimental medicines. *Nature reviews. Neuroscience*, *18*(12), 753–769. https://doi.org/10.1038/nrn.2017.136

Frost, G. R., & Li, Y. M. (2017). The role of astrocytes in amyloid production and Alzheimer's disease. *Open biology*, *7*(12), 170228. https://doi.org/10.1098/rsob.170228

Imran, M., & Mahmood, S. (2011). An overview of human prion diseases. *Virology journal*, *8*, 559. https://doi.org/10.1186/1743-422X-8-559

Kajihara, H., Tsutsumi, E., Kinoshita, A., Nakano, J., Takagi, K., & Takeo, S. (2001). Activated astrocytes with glycogen accumulation in ischemic penumbra during the early stage of brain infarction: immunohistochemical and electron microscopic studies. *Brain research*, *909*(1-2), 92–101. https://doi.org/10.1016/s0006-8993(01)02640-3

Kanashiro, A., Hiroki, C. H., da Fonseca, D. M., Birbrair, A., Ferreira, R. G., Bassi, G. S., Fonseca, M. D., Kusuda, R., Cebinelli, G., da Silva, K. P., Wanderley, C. W., Menezes, G. B., Alves-Filho, J. C., Oliveira, A. G., Cunha, T. M., Pupo, A. S., Ulloa, L., & Cunha, F. Q. (2020). The role of neutrophils in neuro-immune modulation. *Pharmacological research*, *151*, 104580. https://doi.org/10.1016/j.phrs.2019.104580

Katorcha, E., Makarava, N., Savtchenko, R., Baskakov, I. (2015). Sialylation of the prion protein glycans controls prion replication rate and glycoform ratio. *Scientific Reports* **5,** 16912. https://doi.org/10.1038/srep16912

Khosravani, H., Zhang, Y., Tsutsui, S., Hameed, S., Altier, C., Hamid, J., Chen, L., Villemaire, M., Ali, Z., Jirik, F. R., & Zamponi, G. W. (2008). Prion protein attenuates excitotoxicity by inhibiting NMDA receptors. *The Journal of cell biology*, *181*(3), 551–565. https://doi.org/10.1083/jcb.200711002

Kim, I., Mlsna, L. M., Yoon, S., Le, B., Yu, S., Xu, D., & Koh, S. (2015). A postnatal peak in microglial development in the mouse hippocampus is correlated with heightened sensitivity to seizure triggers. *Brain and behavior*, *5*(12), e00403. https://doi.org/10.1002/brb3.403

Kipp, Markus & Amor, Sandra. (2012). FTY720 on the way from the base camp to the summit of the mountain: Relevance for remyelination. Multiple sclerosis (Houndmills, Basingstoke, England). 18. 258-63. 10.1177/1352458512438723.

Le, N., Wu, B., & Harris, D. A. (2019). Prion neurotoxicity. *Brain pathology (Zurich, Switzerland)*, *29*(2), 263–277. https://doi.org/10.1111/bpa.12694

Lehrmann, E., Christensen, T., Zimmer, J., Diemer, N. H., & Finsen, B. (1997). Microglial and macrophage reactions mark progressive changes and define the penumbra in the rat neocortex and striatum after transient middle cerebral artery occlusion. *The Journal of comparative neurology*, *386*(3), 461–476.

Lenz, K. M., & Nelson, L. H. (2018). Microglia and Beyond: Innate Immune Cells As Regulators of Brain Development and Behavioral Function. *Frontiers in immunology*, *9*, 698. https://doi.org/10.3389/fimmu.2018.00698

Li, Q., Cheng, Z., Zhou, L., Darmanis, S., Neff, N. F., Okamoto, J., Gulati, G., Bennett, M. L., Sun, L. O., Clarke, L. E., Marschallinger, J., Yu, G., Quake, S. R., Wyss-Coray, T., & Barres, B. A. (2019). Developmental Heterogeneity of Microglia and Brain Myeloid Cells Revealed by Deep Single-Cell RNA Sequencing. *Neuron*, *101*(2), 207–223.e10. https://doi.org/10.1016/j.neuron.2018.12.006

Liddelow, S. A., Guttenplan, K. A., Clarke, L. E., Bennett, F. C., Bohlen, C. J., Schirmer, L., Bennett, M. L., Münch, A. E., Chung, W. S., Peterson, T. C., Wilton, D. K., Frouin, A., Napier, B. A., Panicker, N., Kumar, M., Buckwalter, M. S., Rowitch, D. H., Dawson, V. L., Dawson, T. M., Stevens, B., … Barres, B. A. (2017). Neurotoxic reactive astrocytes are induced by activated microglia. *Nature*, *541*(7638), 481–487. https://doi.org/10.1038/nature21029

Liddelow, S. A., & Barres, B. A. (2017). Reactive Astrocytes: Production, Function, and Therapeutic Potential. *Immunity*, *46*(6), 957–967. https://doi.org/10.1016/j.immuni.2017.06.006

Mallucci, G., Dickinson, A., Linehan, J., Klöhn, P. C., Brandner, S., & Collinge, J. (2003). Depleting neuronal PrP in prion infection prevents disease and reverses spongiosis. *Science (New York, N.Y.)*, *302*(5646), 871–874. https://doi.org/10.1126/science.1090187

Marella, M., & Chabry, J. (2004). Neurons and astrocytes respond to prion infection by inducing microglia recruitment. *The Journal of neuroscience : the official journal of the Society for Neuroscience*, *24*(3), 620–627. https://doi.org/10.1523/JNEUROSCI.4303-03.2004

McTigue, D. M., & Tripathi, R. B. (2008). The life, death, and replacement of oligodendrocytes in the adult CNS. *Journal of neurochemistry*, *107*(1), 1–19. https://doi.org/10.1111/j.1471-4159.2008.05570.x

Michael, B. D., Bricio-Moreno, L., Sorensen, E. W., Miyabe, Y., Lian, J., Solomon, T., Kurt-Jones, E. A., & Luster, A. D. (2020). Astrocyte- and Neuron-Derived CXCL1 Drives Neutrophil Transmigration and Blood-Brain Barrier Permeability in Viral Encephalitis. *Cell reports*, *32*(11), 108150. https://doi.org/10.1016/j.celrep.2020.108150

Millhauser G. L. (2007). Copper and the prion protein: methods, structures, function, and disease. *Annual review of physical chemistry*, *58*, 299–320. https://doi.org/10.1146/annurev.physchem.58.032806.104657

Nikodemova, M., Kimyon, R. S., De, I., Small, A. L., Collier, L. S., & Watters, J. J. (2015). Microglial numbers attain adult levels after undergoing a rapid decrease in cell number in the third postnatal week. *Journal of neuroimmunology*, *278*, 280–288. https://doi.org/10.1016/j.jneuroim.2014.11.018

Ning, Z. Y., Zhao, D. M., Yang, J. M., Cui, Y. L., Meng, L. P., Wu, C. D., & Liu, H. X. (2005). Quantification of prion gene expression in brain and peripheral organs of golden hamster by real-time RT-PCR. *Animal biotechnology*, *16*(1), 55–65. https://doi.org/10.1081/abio-200053404

Nishida, N., Tremblay, P., Sugimoto, T., Shigematsu, K., Shirabe, S., Petromilli, C., Erpel, S. P., Nakaoke, R., Atarashi, R., Houtani, T., Torchia, M., Sakaguchi, S., DeArmond, S. J., Prusiner, S. B., & Katamine, S. (1999). A mouse prion protein transgene rescues mice deficient for the prion protein gene from purkinje cell degeneration and demyelination. *Laboratory investigation; a journal of technical methods and pathology*, *79*(6), 689–697.

Nutma, E., van Gent, D., Amor, S., & Peferoen, L. (2020). Astrocyte and Oligodendrocyte Cross-Talk in the Central Nervous System. *Cells*, *9*(3), 600. https://doi.org/10.3390/cells9030600

Onodera, T., Sakudo, A., Tsubone, H., & Itohara, S. (2014). Review of studies that have used knockout mice to assess normal function of prion protein under immunological or pathophysiological stress. *Microbiology and immunology*, *58*(7), 361–374. https://doi.org/10.1111/1348-0421.12162

Patel, J., & Balabanov, R. (2012). Molecular mechanisms of oligodendrocyte injury in multiple sclerosis and experimental autoimmune encephalomyelitis. *International journal of molecular sciences*, *13*(8), 10647–10659. https://doi.org/10.3390/ijms130810647

Pham, N., Dhar, A., Khalaj, S., Desai, K., & Taghibiglou, C. (2014). Down regulation of brain cellular prion protein in an animal model of insulin resistance: possible implication in increased prevalence of stroke in pre-diabetics/diabetics. *Biochemical and biophysical research communications*, *448*(2), 151–156. https://doi.org/10.1016/j.bbrc.2014.04.071

Rudd, P. M., Endo, T., Colominas, C., Groth, D., Wheeler, S. F., Harvey, D. J., Wormald, M. R., Serban, H., Prusiner, S. B., Kobata, A., & Dwek, R. A. (1999). Glycosylation differences between the normal and pathogenic prion protein isoforms. *Proceedings of the National Academy of Sciences of the United States of America*, *96*(23), 13044–13049. https://doi.org/10.1073/pnas.96.23.13044

Salter, M. W., & Stevens, B. (2017). Microglia emerge as central players in brain disease. *Nature medicine*, *23*(9), 1018–1027. https://doi.org/10.1038/nm.4397

Salvesen, Ø., Espenes, A., Reiten, M. R., Vuong, T. T., Malachin, G., Tran, L., Andréoletti, O., Olsaker, I., Benestad, S. L., Tranulis, M. A., & Ersdal, C. (2020). Goats naturally devoid of PrP^C are resistant to scrapie. *Veterinary research*, *51*(1), 1. https://doi.org/10.1186/s13567-019-0731-2

Sauvageot, C. M., & Stiles, C. D. (2002). Molecular mechanisms controlling cortical gliogenesis. *Current opinion in neurobiology*, *12*(3), 244–249. https://doi.org/10.1016/s0959-4388(02)00322-7

Schwarz, J. M., Sholar, P. W., & Bilbo, S. D. (2012). Sex differences in microglial colonization of the developing rat brain. *Journal of neurochemistry*, *120*(6), 948–963. https://doi.org/10.1111/j.1471-4159.2011.07630.x

Smith, J. A., Das, A., Ray, S. K., & Banik, N. L. (2012). Role of pro-inflammatory cytokines released from microglia in neurodegenerative diseases. *Brain research bulletin*, *87*(1), 10–20. https://doi.org/10.1016/j.brainresbull.2011.10.004

Stahl, N., Baldwin, M. A., Teplow, D. B., Hood, L., Gibson, B. W., Burlingame, A. L., & Prusiner, S. B. (1993). Structural studies of the scrapie prion protein using mass spectrometry and amino acid sequencing. *Biochemistry*, *32*(8), 1991–2002. https://doi.org/10.1021/bi00059a016

Steele, A. D., Emsley, J. G., Ozdinler, P. H., Lindquist, S., & Macklis, J. D. (2006). Prion protein (PrPc) positively regulates neural precursor proliferation during developmental and adult mammalian neurogenesis. *Proceedings of the National Academy of Sciences of the United States of America*, *103*(9), 3416–3421. https://doi.org/10.1073/pnas.0511290103

Solomon, I. H., Khatri, N., Biasini, E., Massignan, T., Huettner, J. E., & Harris, D. A. (2011). An N-terminal polybasic domain and cell surface localization are required for mutant prion protein toxicity. *The Journal of biological chemistry*, *286*(16), 14724–14736. https://doi.org/10.1074/jbc.M110.214973

Tachibana, M., Mohri, I., Hirata, I., Kuwada, A., Kimura-Ohba, S., Kagitani-Shimono, K., Fushimi, H., Inoue, T., Shiomi, M., Kakuta, Y., Takeuchi, M., Murayama, S., Nakayama, M., Ozono, K., & Taniike, M. (2019). Clasmatodendrosis is associated with dendritic spines and does not represent autophagic astrocyte death in influenza-associated encephalopathy. *Brain & development*, *41*(1), 85–95. https://doi.org/10.1016/j.braindev.2018.07.008

Tang, Y., & Le, W. (2016). Differential Roles of M1 and M2 Microglia in Neurodegenerative Diseases. *Molecular neurobiology*, *53*(2), 1181–1194. https://doi.org/10.1007/s12035-014-9070-5

Thion, M. S., Ginhoux, F., & Garel, S. (2018). Microglia and early brain development: An intimate journey. *Science (New York, N.Y.)*, *362*(6411), 185–189. https://doi.org/10.1126/science.aat0474

Tien, A. C., Tsai, H. H., Molofsky, A. V., McMahon, M., Foo, L. C., Kaul, A., Dougherty, J. D., Heintz, N., Gutmann, D. H., Barres, B. A., & Rowitch, D. H. (2012). Regulated temporal-spatial astrocyte precursor cell proliferation involves BRAF signalling in mammalian spinal cord. *Development (Cambridge, England)*, *139*(14), 2477–2487. https://doi.org/10.1242/dev.077214

Tower, D. B., & Young, O. M. (1973). The activities of butyrylcholinesterase and carbonic anhydrase, the rate of anaerobic glycolysis, and the question of a constant density of glial cells in cerebral cortices of various mammalian

species from mouse to whale. *Journal of neurochemistry*, *20*(2), 269–278. https://doi.org/10.1111/j.1471-4159.1973.tb12126.x

Uschkureit, T., Sporkel, O., Stracke, J., Bussow, H., & Stoffel, W. (2000). Early onset of axonal degeneration in double (plp-/-mag-/-) and hypomyelinosis in triple (plp-/-mbp-/-mag-/-) mutant mice. *The Journal of neuroscience : the official journal of the Society for Neuroscience*, *20*(14), 5225–5233. https://doi.org/10.1523/JNEUROSCI.20-14-05225.2000

van der Knaap, M. S., & Bugiani, M. (2017). Leukodystrophies: a proposed classification system based on pathological changes and pathogenetic mechanisms. *Acta neuropathologica*, *134*(3), 351–382. https://doi.org/10.1007/s00401-017-1739-1

Van Strien, M. E., Baron, W., Bakker, E. N., Bauer, J., Bol, J. G., Brevé, J. J., Binnekade, R., Van Der Laarse, W. J., Drukarch, B., & Van Dam, A. M. (2011). Tissue transglutaminase activity is involved in the differentiation of oligodendrocyte precursor cells into myelin-forming oligodendrocytes during CNS remyelination. *Glia*, *59*(11), 1622–1634. https://doi.org/10.1002/glia.21204

Verkhratsky, A., Ho, M. S., Vardjan, N., Zorec, R., & Parpura, V. (2019). General Pathophysiology of Astroglia. *Advances in experimental medicine and biology*, *1175*, 149–179. https://doi.org/10.1007/978-981-13-9913-8_7

Walter, E. D., Chattopadhyay, M., & Millhauser, G. L. (2006). The affinity of copper binding to the prion protein octarepeat domain: evidence for negative cooperativity. *Biochemistry*, *45*(43), 13083–13092. https://doi.org/10.1021/bi060948r

Wang, H. F., Liu, X. K., Li, R., Zhang, P., Chu, Z., Wang, C. L., Liu, H. R., Qi, J., Lv, G. Y., Wang, G. Y., Liu, B., Li, Y., & Wang, Y. Y. (2017). Effect of glial cells on remyelination after spinal cord injury. *Neural regeneration research*, *12*(10), 1724–1732. https://doi.org/10.4103/1673-5374.217354

Watts, J. C., Bourkas, M., & Arshad, H. (2018). The function of the cellular prion protein in health and disease. *Acta neuropathologica*, *135*(2), 159–178. https://doi.org/10.1007/s00401-017-1790-y

Weissmann, C., Büeler, H., Fischer, M., & Aguet, M. (1993). Role of the PrP gene in transmissible spongiform encephalopathies. *Intervirology*, *35*(1-4), 164–175. https://doi.org/10.1159/000150307

Wu, B., McDonald, A. J., Markham, K., Rich, C. B., McHugh, K. P., Tatzelt, J., Colby, D. W., Millhauser, G. L., & Harris, D. A. (2017). The N-terminus of the prion protein is a toxic effector regulated by the C-terminus. *eLife*, *6*, e23473. https://doi.org/10.7554/eLife.23473

Yang, M., Antoine, D. J., Weemhoff, J. L., Jenkins, R. E., Farhood, A., Park, B. K., & Jaeschke, H. (2014). Biomarkers distinguish apoptotic and necrotic cell death during hepatic ischemia/reperfusion injury in mice. *Liver transplantation : official publication of the American Association for the Study of Liver Diseases and the International Liver Transplantation Society*, *20*(11), 1372–1382. https://doi.org/10.1002/lt.23958

Yang, Y., Higashimori, H., & Morel, L. (2013). Developmental maturation of astrocytes and pathogenesis of neurodevelopmental disorders. *Journal of neurodevelopmental disorders*, *5*(1), 22. https://doi.org/10.1186/1866-1955-5-22

Zhang, B., Shen, P., Yin, X., Dai, Y., Ding, M., & Cui, L. (2020). Expression and functions of cellular prion proteins in immunocytes. *Scandinavian journal of immunology*, *91*(3), e12854. https://doi.org/10.1111/sji.12854